

A STUDY OF ABELL 2146:
DARK AND LUMINOUS

by

Joseph E. Coleman



APPROVED BY SUPERVISORY COMMITTEE:

Lindsay J. King, Chair

Roderick A. Heelis

Mustapha Ishak-Boushaki

Michael Kesden

Copyright © 2018

Joseph E. Coleman

All rights reserved

This is dedicated to Terry.

A STUDY OF ABELL 2146:
DARK AND LUMINOUS

by

JOSEPH E. COLEMAN, AS, BS, MS

DISSERTATION

Presented to the Faculty of
The University of Texas at Dallas
in Partial Fulfillment
of the Requirements
for the Degree of

DOCTOR OF PHILOSOPHY IN
PHYSICS

THE UNIVERSITY OF TEXAS AT DALLAS

May 2018

ACKNOWLEDGMENTS

My sincerest and most gracious thanks go to my advisor, Professor Lindsay J. King, for helping to make all of this possible. It was Professor King that encouraged me to continue my education in the pursuit of a Ph.D. She has helped me in countless ways and has been a wonderful guide during times on this journey that I struggled to find the light. Without Professor King, none of this would be possible.

I also would like to thank my Supervisory Committee, Professors Roderick A. Heelis, Mustapha Ishak-Boushaki, and Michael Kesden. Their support, patience, and kind consideration is greatly appreciated.

Everyone in the UTD Cosmology, Relativity, and Astrophysics Group during my time as a graduate student has my thanks. I appreciate having been able to work with Miyoung Choi, Matthew Fong, and Brandyn Lee. Thanks to Eske Pedersen for chats about GADGET-2. Thanks to Jacob White for listening to me complain about LENSTOOL. I also want to thank all my collaborators. They have been a tremendous help.

I had the special privilege during my time at UTD to have been a student of Professor Wolfgang Rindler. It is an amazing honor to have been taught the theory of relativity by him. Our conversations about the nature of spacetime are cherished.

The material contained in this dissertation was in part supported by a grant from Space Telescope Science Institute program 12871, by a grant from the National Science Foundation, number 1517954, by NASA through a Fellowship of the Texas Space Grant Consortium, by World Premier International Research Center Initiative (WPI Initiative), MEXT, Japan, and JSPS KAKENHI Grant Number 26800093 and 15H05892. The author acknowledges the Texas Advanced Computing Center (TACC) at The University of Texas at Austin for providing HPC resources that have contributed to the research results reported within this dissertation. (www.tacc.utexas.edu). This work used the COSMA Data Centric system at Durham

University, operated by the Institute for Computational Cosmology on behalf of the STFC DiRAC HPC Facility (www.dirac.ac.uk). This equipment was funded by a BIS National E-infrastructure capital grant ST/K00042X/1, DiRAC Operations grant ST/K003267/1 and Durham University. DiRAC is part of the National E-Infrastructure.

My friends and family have been big supporters throughout this endeavor and I am thankful to you all. My gratitude goes to Carol Hegg for being an amazing supporter. Most of all, the encouragement, patience, love, and understanding from Terry Hegg is difficult to state in words. Terry brings me my coffee when I'm working late. There is no better person in the universe. Thank you.

April 2018

A STUDY OF ABELL 2146:

DARK AND LUMINOUS

Joseph E. Coleman, PhD
The University of Texas at Dallas, 2018

Supervising Professor: Lindsay J. King, Chair

The universe is a highly dynamic system. Under the primary influence of gravity, matter in the universe clumped together to create the structure we currently observe with our telescopes. Gravity formed objects on vastly different scales, from planets and stars that form solar systems, to vast collections of star systems that comprise galaxies, and then collections of galaxies to create the largest gravitationally bound objects in the universe, galaxy clusters.

The structure we see in the universe forms hierarchically in the sense that two smaller objects come together under the influence of gravity and create something bigger. Here we study one such merging event in the galaxy cluster Abell 2146. It is a rare system given that it appears that the time since the two galaxy clusters crashed into one another is rather short in the scheme of the universe. Abell 2146 is also positioned at just the orientation in the sky that we can observe the collision from the side. This gives us a great view of the galaxies, the dark matter, and the intervening plasma between the galaxies that give off X-rays.

We localize the position of the dark matter component in the cluster by use of gravitational lensing. We construct models that act as a lens that distorts the light from background galaxies. By looking at how the light is distorted, we reconstruct the location of dark matter in the system in tandem with the regular ordinary matter. This gave the exciting result

that the bright peak in the X-ray signal coming from the plasma or intracluster medium was traveling in front of the more massive component of the system, which is unique among the few systems that exist like this.

In an attempt to understand what could have caused this strange configuration, hydrodynamic simulations were performed using simple density profiles as proxies for the dark matter and plasma that make up the bulk of galaxy clusters. Constraints were obtained from previous studies to reduce the explored parameter space. Mock X-ray maps were generated from simulation results and compared to observations from the *Chandra X-ray Observatory*. We find there must be some additional physics needed that was not implemented in the simulations or some unknown starting condition to match certain features observed in X-ray. We obtained simulation results where we see a bright X-ray peak ahead of the more massive cluster but without shock fronts and also at a much later time in the evolution of the system than what was originally thought.

TABLE OF CONTENTS

ACKNOWLEDGMENTS	v
ABSTRACT	vii
LIST OF FIGURES	xi
LIST OF TABLES	xiv
CHAPTER 1 ON THE ORIGIN OF THE UNIVERSE	1
1.1 Introduction	1
1.2 Cosmology	1
1.3 Structure	3
CHAPTER 2 ABELL 2146	5
CHAPTER 3 INTRODUCTION TO RESEARCH OF ABELL 2146	9
CHAPTER 4 STRONG LENSING OF ABELL 2146	11
4.1 Introduction	11
4.2 Lensing Theory	13
4.3 Observations and Data Reduction	16
4.4 Lens Models	18
4.5 Procedure	21
4.5.1 Cluster Member Selection	21
4.5.2 Model Refinement	22
4.5.3 Multiple Image Detection	23
4.6 Lens Model Constraints	27
4.7 Computation	28
4.8 Results and Discussion	29
4.8.1 Model 1	32
4.8.2 Model 2	32
4.8.3 Model 3	33
4.8.4 Other Models	33
4.9 Conclusion	37

CHAPTER 5	HYDRODYNAMIC SIMULATIONS OF ABELL 2146	39
5.1	Introduction	39
5.2	Simulation Background and Theory	39
5.3	Initial Conditions	41
5.3.1	Hernquist Density Profile	41
5.4	Data	47
5.4.1	Particle Counts	47
5.4.2	Simulation Runtime	47
5.5	Procedure and Analysis	48
5.5.1	Finding Peaks	50
5.5.2	Generating X-ray maps	51
5.6	Results and Analysis	53
5.7	Conclusion	57
CHAPTER 6	SUMMARY AND CONCLUDING REMARKS	60
REFERENCES	62
BIOGRAPHICAL SKETCH	69
CURRICULUM VITAE		

LIST OF FIGURES

1.1	A computer simulation of structure formation where I have identified structures and clusters with machine learning. The different colors represent different classifications of data, according to a machine learning algorithm, indicative of structure formation. The data used in the machine learning algorithm is adapted from a publicly available subset of the “Millennium Run” (Springel et al., 2005; Lemson and Virgo Consortium, 2006).	4
2.1	A false color image from the <i>Hubble Space Telescope</i> of Abell 2146.	6
4.1	A false color view of a <i>Hubble Space Telescope</i> of the brightest cluster galaxy in cluster A. There are two prominent strong lensing features with distinct bilateral symmetry, the ‘mask’ system and the ‘bra-ket’ system. The mask system has two emission knots that look like eyes. The bra-ket system resemble the symbols < and >. Southeast of the center of BCG-A is a jet of gas from the active galactic nucleus.	12
4.2	A diagram illustrating the deflection of a light ray by a gravitational lens. Image Credit: (Schneider, 2003)	14
4.3	Note the rotation; north is towards the bottom right and east is towards the top right. Multiple image systems used as constraints in the vicinity of BCG-A. Identical objects have the same letter prefix, e.g. ‘a1,’ ‘a2,’ and ‘a3.’ The color grouping indicates the objects considered to be at the same redshift. Objects ‘a,’ ‘c,’ and ‘d’ are in cyan. Objects ‘e’ and ‘f’ are in green. Object ‘j’ is in magenta. Objects ‘g,’ ‘h,’ and ‘m’ are in red. The set a, c, and d was statically assigned a redshift of $z = 2.0$. Other systems were assumed to have a flat prior for the redshift in the range $z = 0.3$ to $z = 3.0$	17
4.4	A false color picture of Abell 2146. The f814W filter was mapped to the color red, f606W filter was mapped to green, and f435W was mapped to blue. The circles indicate cluster members that are modeled as Pseudo Isothermal Elliptical Mass Distribution (PIEMD) perturbers. BCG-A and BCG-B indicate the brightest cluster galaxies in each of the respective clusters. The location of point C is where a mass overdensity appears in the weak lensing analysis (King et al., 2016). Circle size has no meaning.	19
4.5	Perturbers to the lens model are plotted as green squares; all other galaxies are plotted as points. On the vertical, axis color is computed from SExtractor (Bertin and Arnouts, 1996) aperture magnitudes, 40 pixel diameter. The horizontal axis is SExtractor auto magnitudes. Magnitudes are computed from <i>HST</i> images. A trend line is plotted through the perturbers with additional lines above and below to show ± 0.5 shift in color of the trend line All of the perturbers are on the red sequence for the cluster.	22

4.6	Close-up view of a false color image of the ‘mask.’ This system is east of BCG-A. This feature exhibits a bilateral symmetry.	23
4.7	From the f606W filter, a close-up view of a high contrast image of the ‘bra-ket’ images, called so because the shape resembles ‘<’ and ‘>.’ In the top panel, the bilateral symmetry is evident and in the bottom panel there is a 3rd counter image. The symmetric pair is located west of BCG-A and the third counter image is northeast of BCG-A. The ‘bra-ket’ system is modeled with points a , c , and d . The blue pair next to ‘<’ and ‘>’ is modeled with points e and f	24
4.8	In the vicinity of BCG-A, group G1 is the test point in the image plane. Groups G2 through G5 are counter images of G1 parametrized by redshift. The position of an image, G1, is projected from the image plane to the source plane at varying redshifts. The resulting source plane positions of G1 at varying redshifts are then projected onto the lens plane. The multiplicity of an image is dependent on redshift. This results in various predictions of multiple images in groups G2 through G5 as functions of assumed redshift of the source of the image in group G1. Group G2 begins at a redshift of $z = 0.9$, group G3 begins at $z = 0.7$, and groups G4 and G5 begin to appear at a redshift of $z = 1.7$	26
4.9	In the left frame, an expanded view of the region around G2 in Figure 4.8. There is a blue galaxy as a possible counter image for some assumed redshift of G1 slightly less than $Z = 1.3$ for some intermediate mass model. The counter images in this group have an increasing redshift in the northeast direction. In the right frame, a blue galaxy in group G3 appears as a possible counter image for the same assumed redshift of G1 between the same range of redshifts as the galaxy in the left frame. Both of these galaxies are on the redshift parametrized path at the same z location.	27
4.10	The red star is the center of the BCG-A as determined with SExtractor and the blue diamond is the peak of the hot X-ray gas (Russell et al., 2010, 2012). The collection of black points near the BCG-A center is a plot of the centroid of dark matter halo for 1000 samples from the best fit lens model. North is up and east is left. Top image is model 1, middle image is model 2, and bottom image is model 3. BCG-B is out of the frame to the northwest (or top right) direction from BCG-A. The contours are from <i>Chandra X-ray Observatory</i> with a 3 pixel Gaussian smoothing. Note that the second X-ray peak coincident with BCG-A is a point source associated with the AGN of the BCG. This is not a gas peak. The X-rays from this point source are non-thermal (Russell et al., 2012).	36
5.1	Differences in density, ρ , due to different parameter matching schemes are plotted. A target NFW profile of mass $M_{200} = 1.1 \times 10^{15} M_{\odot}$ and concentration $c = 3.5$ is the blue curve. The orange curve more closely matches the NFW profile up to the NFW R_{200} radius, which is the matching prescribed by Robertson et al. (2017) and also used here. The matching scheme used by Springel et al. (2005) (green curve) is not as close of a match to the NFW up to the R_{200} radius. The plot is from 10 kpc to R_{200}	44

5.2	A comparison between two formulas for calculating the energy per unit mass. Equation 5.13 is the “1D σ ” line plot, and equation 5.14 is the “integral” circle plot.	46
5.3	The separation distance between peaks in the dark matter. Time is on the vertical axis, distance on the horizontal axis. Core passage occurs at roughly $t = 1.7$ in internal time units. The more massive halo A starts on the right at time $t = 0$ at location $X = 2500$ kpc. Halo B starts at $x = -2500$ kpc and is on the left. At the end of the simulation halo A is on the left and halo B is on the right. . . .	49
5.4	Left hand side, in the plane of the sky we see objects separated by some distance. Right hand side, two objects can have a separation larger than observed if tilted some angle θ with respect to the surface their positions are projected on, in this case, the plane of the sky.	49
5.5	Left, a slice of pixel counts from the X-ray data obtained from <i>Chandra X-ray Observatory</i> . The vertical line on the left is the location of BCG-A, the vertical line on the right is the location of BCG-B. The upstream shock front is coincident with BCG-B. The bow shock is to the left of the X-ray peak. The sharp spike at the location of BCG-A is due to an active galactic nuclei. Right, the X-ray image of Abell 2146. The bright peak is in the lower left of the image.	53
5.6	The more massive halo A starts at 2500 kpc, the less massive halo B starts at -2500 kpc. The halo A concentration is constant in each of the plots while the halo B concentration is 2.0, 3.5, and 5.0.	55
5.7	Plotted are the separation distances versus simulation time for all combinations of concentrations where the mass ratio is 11:3.5. The more massive halo A starts at 2500 kpc, the less massive halo B starts at -2500 kpc. The behavior of halo B varies more after collision than does halo A.	56
5.8	The more massive halo A starts at 2500 kpc, the less massive halo B starts at -2500 kpc. The halo B concentration is constant in each of the plots while the halo A concentration is 2.0, 3.5, and 5.0.	57
5.9	The best fit according to our χ^2 calculation gives parameters $c_A = 3.5$, $c_B = 2.0$. The black triangles indicate the locations of the peaks in the dark matter from observation. The green triangles mark the locations of the dark matter peaks in the simulation.	58
5.10	For concentrations $c_A = 5.0$ and $c_B = 2.0$ the peak in X-ray is ahead of the peak in dark matter. The black triangles indicate the locations of the peaks in the dark matter from observation. The green triangles mark the locations of the dark matter peaks in the simulation.	58

LIST OF TABLES

4.1	Parameters of an L^* elliptical galaxy used in scaling relations. The parameter m_0^* is apparent magnitude, σ_0^* is velocity dispersion, r_{cut}^* is cut radius, and r_{core}^* is core radius. The core radius is a fixed value.	21
4.2	Comparison of distinguishing features between lens models 1, 2, and 3. Mass is given in units of $10^{15}M_\odot$. All parameters of halo B and halo C are fixed.	34
4.3	Comparison of results from lens models 1, 2, and 3. The Mean Position is for the dark matter centroid. The error matrix shows the variance and covariance of the dark matter halo position. The separations are between the mean position of the dark matter centroid and either the peak light position of BCG-A or the X-ray peak. The $\text{Ln}(\text{Evidence})$ for Model 2 yields a significant Bayes factor (Trotta, 2008) relative to either of the other models.	37
5.1	Particle counts for two halos, A and B, where A is more massive than B, and varying concentrations of A. The halo with the smaller M_{200} determines the particle mass such that there are a total of 10^6 particles inside the volume determined by the corresponding R_{200} . The particle count of the other halo adjusts to this requirement.	47

CHAPTER 1

ON THE ORIGIN OF THE UNIVERSE

1.1 Introduction

This dissertation is organized as follows: Chapter 1 gives a brief introduction to cosmology. Chapter 2 introduces the system Abell 2146. Chapter 3 details research that others and I have done. Chapter 4 details current research done involving strong gravitational lensing. Chapter 5 details hydrodynamic simulations of Abell 2146. Concluding remarks can be found in Chapter 6.

1.2 Cosmology

“Bang” said the universe.

Or so that is the current widely held theory—that the age of the universe is about 13.8 Gyr and it was in an initial state of high temperature and density (Dodelson, 2003). From a statistical mechanics perspective, the universe can be described by the synthesis of nuclei as the universe cools and expands. The interaction cross section and binding energies of various components allow for forming a model of the universe (Pathria and Beale, 2011; Dodelson, 2003). This is known as “Big Bang Nucleosynthesis.”

With this initial configuration of energy and matter we assume that the universe is both isotropic and homogeneous on sufficiently large scales. This assumption about the matter in the early universe being evenly distributed and smooth in all directions can be used to solve Einstein’s field equations of general relativity. From Einstein we have

$$R_{\alpha\beta} - \frac{1}{2}g_{\alpha\beta}R + \Lambda g_{\alpha\beta} = \frac{8\pi G}{c^4}T_{\alpha\beta}, \quad (1.1)$$

where $R_{\alpha\beta}$ is the Ricci tensor, R the Ricci scalar, $g_{\alpha\beta}$ the metric, Λ the cosmological constant, G Newton’s gravitational constant, c the speed of light, and $T_{\alpha\beta}$ the stress-energy tensor.

The left hand side of equation 1.1 describes the curvature of spacetime and the right hand side describes the matter content. With the idea that the matter content of the universe is smooth and the same in every direction, it can be described as a perfect fluid with some density ρ and some pressure P . This is enough to specify the stress-energy tensor to obtain a solution to Einstein's field equation. The stress-energy tensor is, for a perfect fluid,

$$T_{\alpha\beta} = (\rho + P)u_{\alpha}u_{\beta} + Pg_{\alpha\beta},$$

where u_{α} is the 4-velocity vector of the fluid.

The solution for such a smooth universe turns out to be one that can experience expansion. This simple, expanding universe is described by a Friedman-Lemaître-Robertson-Walker (FLRW) metric,

$$ds^2 = -c^2dt^2 + a(t)^2(dx^2 + dy^2 + dz^2),$$

where $a(t)$, the scale parameter, is a function that describes the expansion of the universe and is dependent on matter density, pressure, dark energy, and curvature (Dodelson, 2003).

From the scale parameter we can define a cosmological redshift as

$$1 + z = \frac{a_0}{a(t)}, \tag{1.2}$$

where z is the redshift and a_0 is scale parameter of the universe at the current time and is taken have the numerical value $a_0 = 1$. As the space in the universe expands, any waves, such as light, will expand as well. This elongation of the wavelength of light will shift the color light. Blue light that experiences a redshift will change color towards the red end of the visible spectrum, hence the name redshift.

The scale parameter $a(t)$ and the rate of change of the scale parameter $\dot{a}(t)$, where the dot denotes the time derivative, both define the Hubble parameter $H(t)$ as

$$H(t) = \frac{\dot{a}(t)}{a(t)}.$$

Within the FLRW cosmology, the Hubble parameter can be expressed in terms of redshift z as

$$H(z) = H_0 \sqrt{\Omega_m(1+z)^3 + \Omega_k(1+z)^2 + \Omega_\Lambda},$$

where Ω_m , Ω_k , and Ω_Λ are parameters that describe the percentages of matter, curvature, and dark energy respectively at the current time in the universe, and H_0 is the Hubble constant which is the Hubble parameter at the current time. For a flat universe with no curvature we have $\Omega_k = 0$. The modern picture of the universe obtained from observations gives, for the remaining parameters, $\Omega_m \approx 30\%$, $\Omega_\Lambda \approx 70\%$ and $H_0 \approx 70$ kilometers per second per megaparsec (Dodelson, 2003).

1.3 Structure

Although we start with a smooth and uniform density in the universe, there are however, on small scales, fluctuations in density which gave rise to the cosmic microwave background (CMB) anisotropies (Smoot et al., 1992; Pathria and Beale, 2011) as the universe expands and cools. These fluctuations are the seeds for structure formation in the universe. Under the influence of gravity, on the largest scales of structure there are large voids surrounded by filaments of galaxies. The filaments are tied together at nodes where large clusters of galaxies reside. Figure 1.1 illustrates the structure of the universe.

There is a large amount of data that is consistent with a universe comprised of dark energy in the form of the cosmological constant (Λ from general relativity) and cold dark matter¹ (Ostriker and Steinhardt, 1995; Dodelson et al., 1996). This paradigm is generally referred to as Λ CDM (Ostriker and Steinhardt, 1995; Dodelson et al., 1996).

As the universe continues to evolve, collections of gravitationally bound galaxies, called clusters, merge hierarchically to form structure. When large clusters of galaxies collide we

¹Hereafter, CDM stands for “cold dark matter”, and DM stands for “dark matter.”

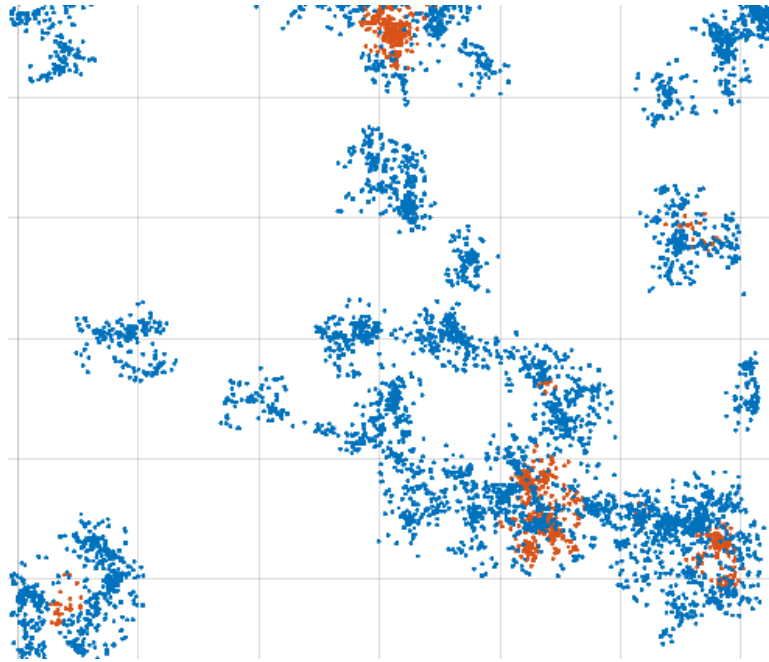


Figure 1.1. A computer simulation of structure formation where I have identified structures and clusters with machine learning. The different colors represent different classifications of data, according to a machine learning algorithm, indicative of structure formation. The data used in the machine learning algorithm is adapted from a publicly available subset of the “Millennium Run” (Springel et al., 2005; Lemson and Virgo Consortium, 2006).

can use them as a way to study the physical properties of the universe, such as the validity of Λ CDM, by mapping peaks in density fluctuations, the nature of dark matter (Allen et al., 2011), and even the magnetohydrodynamics of hot, dilute plasmas (Kunz et al., 2011).

CHAPTER 2

ABELL 2146

Some of the work contained in this chapter originally appeared in “The mass distribution of the unusual merging cluster Abell 2146 from strong lensing,” Joseph E. Coleman, Lindsay J. King, Masamune Oguri, Helen R. Russell, Rebecca E. A. Canning, Adrienne Leonard, Rebecca Santana, Jacob A. White, Stefi A. Baum, Douglas I. Clowe, Alastair Edge, Andrew C. Fabian, Brian R. McNamara, Christopher P. O’Dea (2017), *Monthly Notices of the Royal Astronomical Society*, Volume 464, Issue 2, p. 2469-2480, and is reproduced by permission of Oxford University Press. All writing and work was performed by JEC with edits and feedback provided by coauthors. Access and instruction was provided by MO for the private GLAFIC lensing software.

The cluster system Abell 2146, as seen in Figure 2.1, was first discovered to consist of two massive clusters undergoing a major merger by Russell et al. (2010), with an appearance on *Chandra X-ray Observatory* images reminiscent of the Bullet Cluster (e.g. Clowe et al., 2006) (e.g. Clowe et al. 2006). On X-ray images, the system is unique in presenting within the intracluster medium (ICM), which is a plasma, two large shocks of Mach number ~ 2 (Russell et al., 2010, 2012), indicative of a relatively recent¹ merger between two clusters more similar in mass than those in the Bullet Cluster. Estimates from X-ray analysis (Russell et al., 2010, 2012) and dynamical analysis (White et al., 2015) are consistent with a merger observed about 0.1-0.2 Gyr after first core passage, recent on the dynamical time scales of clusters. Abell 2146 holds great promise for investigating the transport processes in the plasma in cluster environments (Russell et al., 2012).

¹Recent in the context of cosmological time scales is less than 0.3 Gigayears.

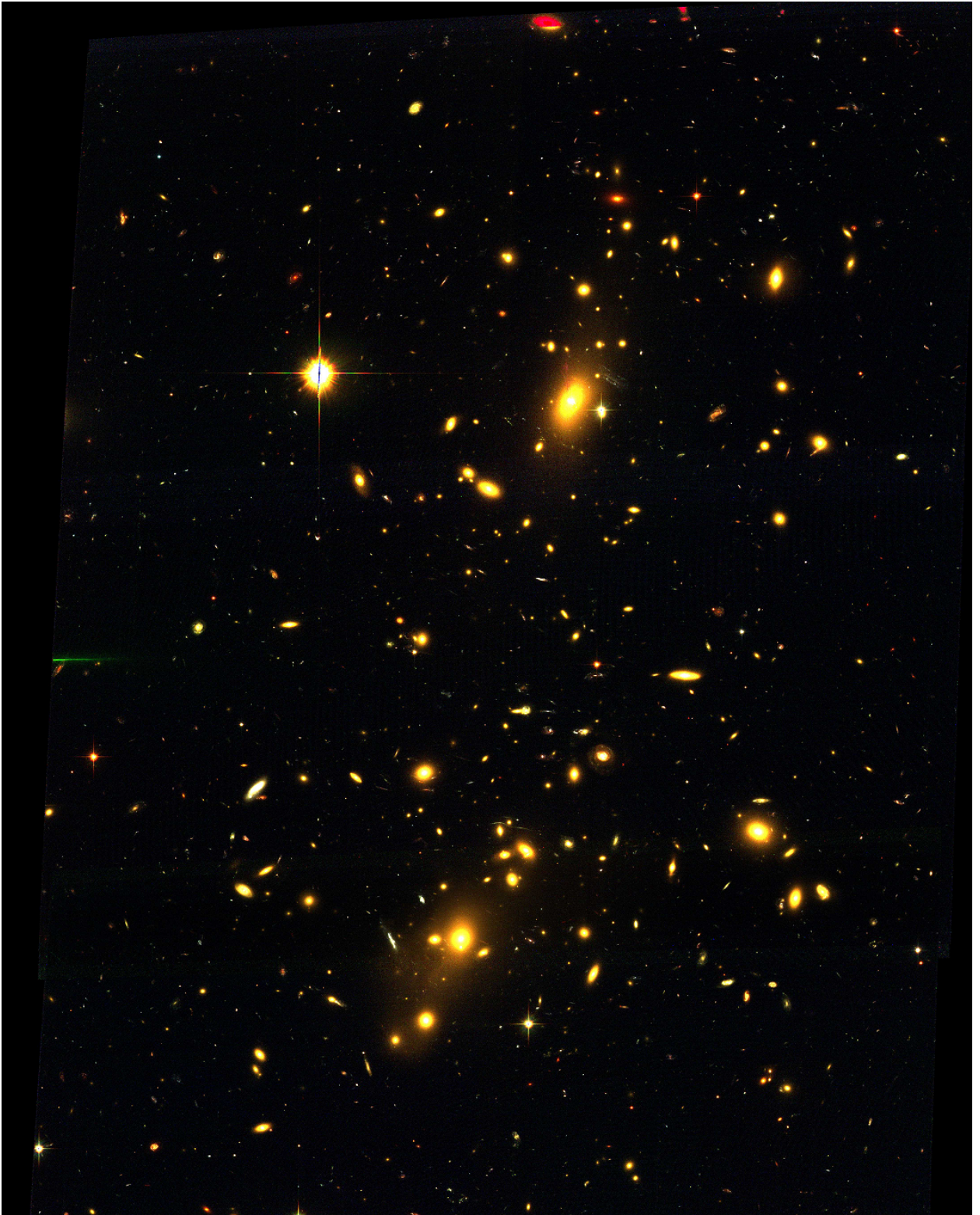


Figure 2.1. A false color image from the *Hubble Space Telescope* of Abell 2146.

Dark matter accounts for about 85% of the mass of galaxy clusters. Most of the baryonic² mass, accounting for about 15% of the total gravitating mass, is hot X-ray emitting plasma, and at most a few percent of the total mass resides in the stellar components of galaxies. Major mergers of galaxy clusters occurring close to the plane of the sky³ are very rare events, and their importance in cosmology has been highlighted by the findings from the first such system to be discovered, the Bullet Cluster (1E0657–558; e.g. Clowe et al. 2006; Markevitch and Vikhlinin 2007). In such systems that have recently collided, the intracluster medium can form shock fronts which allow the study of physical processes in the plasma (Macario et al., 2011). The Bullet Cluster is regarded as compelling evidence for the existence of dark matter and is a cosmological laboratory for testing the interaction cross section of dark matter with itself and with ordinary matter (Markevitch et al., 2002; Clowe et al., 2004, 2006; Markevitch et al., 2004).

When clusters collide, the clouds of hot plasma are slowed down by ram pressure. The galaxies are essentially collisionless because the separation distance between galaxies is large compared to their size. Galaxies are affected mainly by tidal interactions and dynamical friction (Chandrasekhar, 1949). Dark matter also does not have a large cross-section for interaction (e.g. Markevitch et al. 2004; Randall et al. 2008; Harvey et al. 2015) with either itself or with ordinary matter. So, shortly after collision, the major concentrations of galaxies and the dark matter are expected to lead the plasma clouds (e.g. Clowe et al. 2006). A major merger thus results in a dissociation between the plasma clouds, galaxies, and dark matter, the specifics of which depend on the cluster properties and merger geometry.

²In cosmology, the term “baryons” is a catchall term used to differentiate between dark matter and everything else. Baryonic matter is any matter that can interact electromagnetically.

³We see the universe as a projection on the night sky. For two objects to be in the plane of the sky with respect to each other means they are side by side. For two objects not in the plane of the sky, one can be further behind the other, but since we see in projection, we can not know for sure which is in front of the other.

A cool core of a galaxy cluster is formed from the gas in the halo contracting into a dense region that cools by radiating energy away, typically as X-rays, and experiences a flow of matter inward to take the place of gas that has contracted into the dense core (Hudson et al., 2010).

The X-ray cool core of the cluster component Abell 2146-A (Russell et al., 2010, 2012) is offset from the Brightest Cluster Galaxy (BCG) seen on *Hubble Space Telescope* images (King et al., 2016; Canning et al., 2012), but it leads, rather than lags, the BCG in their trajectories (Russell et al., 2010, 2012). At a later stage in a merger, a gravitational slingshot that causes the plasma to overtake the dark matter and galaxies is possible (Hallman and Markevitch, 2004) but the merger would have to be seen a factor of several times later since first core passage for this explanation to be dynamically viable (Russell et al., 2012). Weak lensing mass reconstruction (King et al., 2016) using the distorted shapes of background galaxies on *Hubble Space Telescope* images is consistent with the peak in the dark matter in Abell 2146-A being offset from the X-ray cool core, but the resolution of the mass map is too low to draw a statistically robust conclusion. The galaxies in Abell 2146-B are located ahead of the peak in the plasma density, with the BCG being almost coincident with one of the X-ray shocks.

CHAPTER 3

INTRODUCTION TO RESEARCH OF ABELL 2146

There have been a number of studies of Abell 2146.

Russell et al. (2010, 2012) used observations from *Chandra X-ray Observatory* and identified two large shock fronts in the intracluster medium indicating that a cluster merger had occurred. Abell 2146 is one of very few merger systems with defined shock fronts in X-ray.

Canning et al. (2012) observed Abell 2146 with the Optically Adaptive System for Imaging Spectroscopy. From their spectroscopic analysis they observed a large plume of gas emanating from the brightest cluster galaxy (BCG) in cluster Abell 2146-A pointed in the direction of the X-ray peak. Several scenarios were offered as an explanation of this gas plume such as tidal striping from another galaxy and also ram pressure striping of the gas internal to the BCG.

White et al. (2015), for which I am a coauthor, looked at spectroscopic data of the cluster merger and performed a dynamical analysis in order to determine mass of the system and time scale of the merger. From the redshift data a velocity dispersion was obtained. This velocity dispersion was then used to calculate the mass of the system by using the virial theorem. Additionally, a two-body dynamical model was considered to estimate projected angle from the sky, infall velocity, and separation distance.

AMI Consortium et al. (2011) observed the cluster in the range of 13.9-18.2 GHz with the Arcminute Microkelvin Imager. This was a temperature map of the Sunyaev-Zel'dovich (SZ) effect. The SZ effect is the inverse Compton scattering of the cosmic microwave background photons as they pass through plasmas with more energetic electrons. The SZ observations when compared to the X-ray data from (Russell et al., 2012) were found to have offsets in peaks between the two signals concluding that this is the result of complex dynamics from a merger event.

King et al. (2016), for which I am a coauthor, performed a weak lensing analysis of Abell 2146 using observations taken from *Hubble Space Telescope*. In this analysis the weak lensing maps indicated a third overdensity from the background in the cluster. This was concluded to be noise in the data.

Stevenson et al. (prep), a UTD undergrad, performed parameter estimation using publicly available code, MCMAC (Dawson, 2014). Priors on subcluster mass, radial velocity, and projected separation are used in an analytic model to determine collision velocity, time since collision, etc.

Russell et al. (2011) did not find any extended radio emission using the Giant Metrewave Telescope. Recent observations by Hlavacek-Larrondo et al. (2018) using the Karl G. Jansky Very Large Array has detected a faint radio signal. Specifically, two extended radio sources were found, one associated with BCG-A and one near BCG-B (Hlavacek-Larrondo et al., 2018).

CHAPTER 4

STRONG LENSING OF ABELL 2146

Some of the work contained in this chapter originally appeared in “The mass distribution of the unusual merging cluster Abell 2146 from strong lensing,” Joseph E. Coleman, Lindsay J. King, Masamune Oguri, Helen R. Russell, Rebecca E. A. Canning, Adrienne Leonard, Rebecca Santana, Jacob A. White, Stefi A. Baum, Douglas I. Clowe, Alastair Edge, Andrew C. Fabian, Brian R. McNamara, Christopher P. O’Dea (2017), *Monthly Notices of the Royal Astronomical Society*, Volume 464, Issue 2, p. 2469-2480, and is reproduced by permission of Oxford University Press. All writing and work was performed by JEC with edits and feedback provided by coauthors. Access and instruction was provided by MO for the private GLAFIC lensing software.

4.1 Introduction

Presented here is the strong lensing analysis of Abell 2146 using multiple image systems, some of which are shown in Figure 4.1, identified on *Hubble Space Telescope* images. In particular, we focus on the distribution of mass in Abell 2146-A in order to determine the centroid of the total mass and of the dark matter (DM) halo. We use object colors and morphologies to identify multiple image systems; very conservatively, four of these systems are used as constraints on a lens mass model. We find that the centroid of the total mass and of the dark matter halo, constrained using the strongly lensed features, are coincident with the brightest cluster galaxy (hereafter BCG), with an offset of ≈ 2 kpc between the centers of the dark matter halo and the BCG. With the determination of the dark matter centroid from the strong lensing model, we ascertained that the X-ray cool core also leads the dark matter centroid in Abell 2146-A, with an offset of ≈ 30 kpc.

This is an unexpected result, but is consistent with the relative locations of the cool core and BCG in Abell 2146-A. In a collision of galaxy clusters the dark matter components

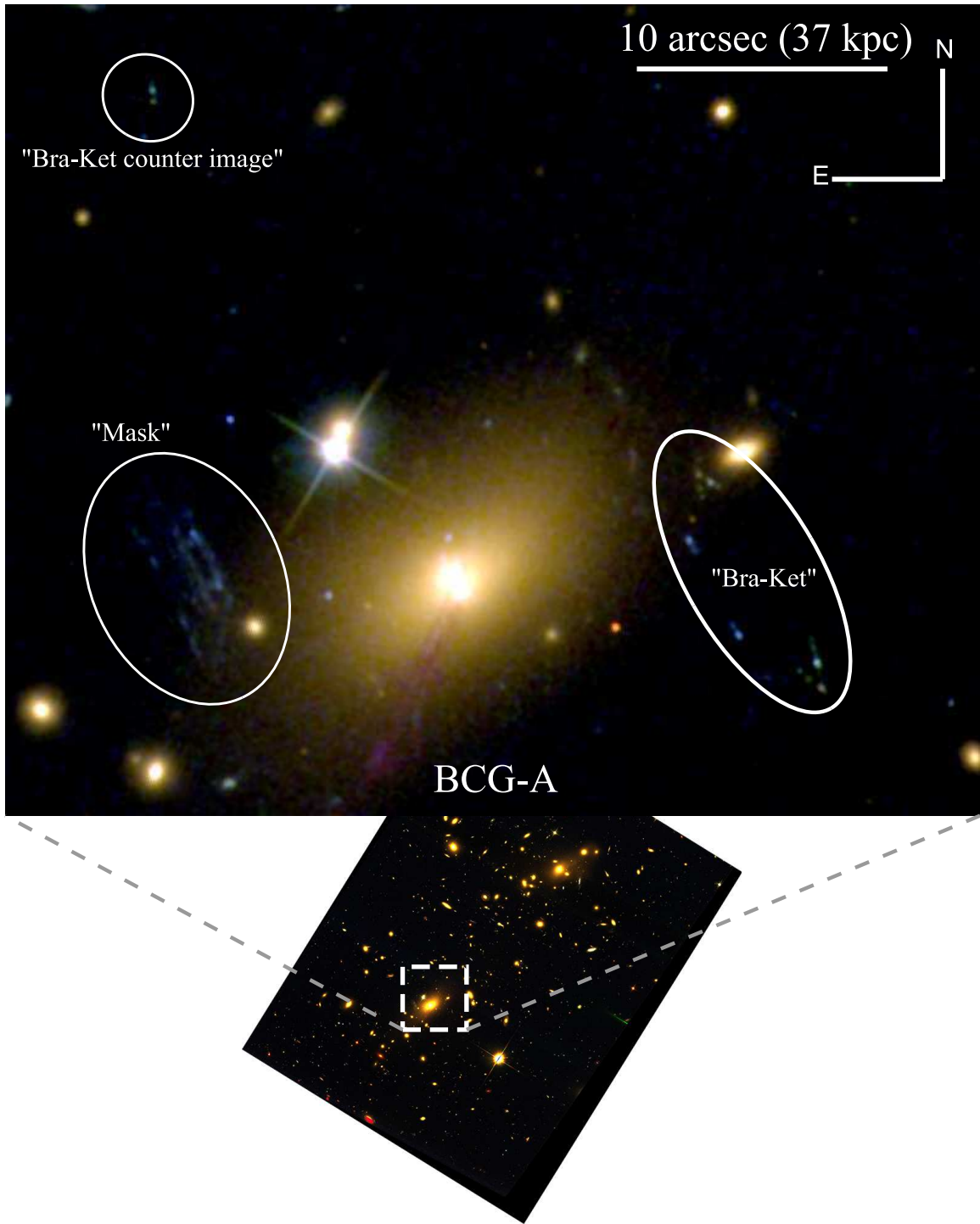


Figure 4.1. A false color view of a *Hubble Space Telescope* of the brightest cluster galaxy in cluster A. There are two prominent strong lensing features with distinct bilateral symmetry, the ‘mask’ system and the ‘bra-ket’ system. The mask system has two emission knots that look like eyes. The bra-ket system resemble the symbols < and >. Southeast of the center of BCG-A is a jet of gas from the active galactic nucleus.

have very small interaction cross sections with either dark matter or ordinary matter. The dark matter components are expected to pass through the other components, both dark and baryon, with the only effects on them being tidal gravitational forces and dynamical friction (Chandrasekhar, 1949). The intracluster medium (ICM) is composed of hot, sparse plasma. In a collision, the ICM components of clusters are expected to collide, and through ram pressure, heat up. The signature of this is evident in the bullet cluster where, after collision, the dark matter components pass through everything and are on other side of the hot gas components (Markevitch et al., 2002; Clowe et al., 2004, 2006; Markevitch et al., 2004).

The configuration of Abell 2146-A is that the hot gas is leading both the brightest cluster galaxy and the dark matter centroid.

4.2 Lensing Theory

Gravitational lensing is the deflection of light due to a mass distribution. The deflection is sensitive to all types of mass, so it can measure the distributions of both baryonic (normal) matter and dark matter (Schneider, 2003). Figure 4.2 is a diagram of a typical lens model. An observer sees light that has passed through a mass distribution, the lens, some distance¹ D_d away. This light, which originates from some source a distance D_s away from the observer, is deflected by the lens by an angle α . The distances separating the observer, the lens, and the sources are all much larger than the physical size of the mass distribution which allows for considering the mass as a thin lens.

The lens equation to be solved is

$$\vec{\beta} = \vec{\theta} - \vec{\alpha}(\vec{\theta}),$$

where $\vec{\beta}$ is the angle to the real source at some position $\vec{\eta}$ in the source plane, $\vec{\theta}$ is the angle at which the deflected image in the lens plane appears at location $\vec{\xi}$, and $\vec{\alpha}(\vec{\theta})$ is the scaled

¹Angular diameter distance. See Hogg (1999) for distinctions in distance measures.

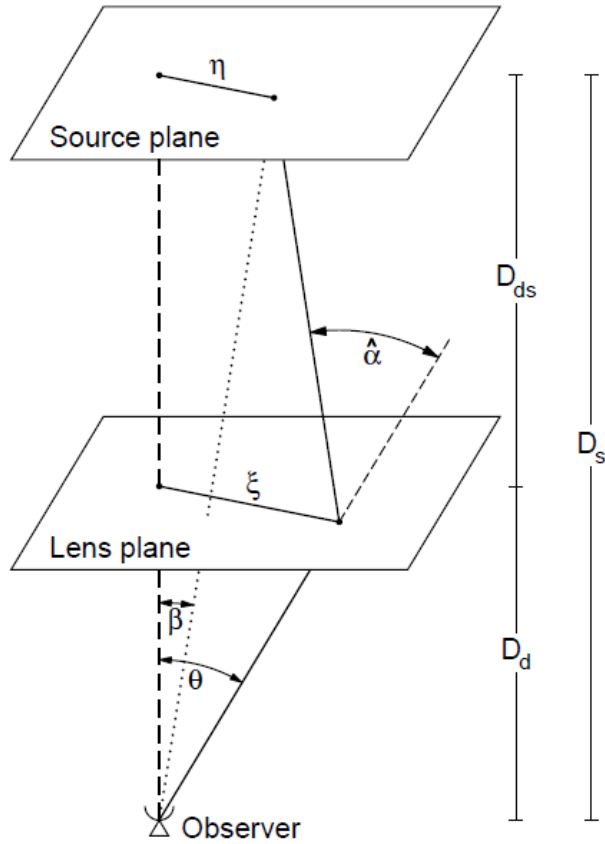


Figure 4.2. A diagram illustrating the deflection of a light ray by a gravitational lens. Image Credit: (Schneider, 2003)

deflection angle in terms of a dimensionless surface mass density (Schneider, 2003). The surface mass density of the lens is a projection of the 3D density profile along the line of sight since our observations are of this projection.

The surface mass density is Σ , calculated by summing the mass along one direction as

$$\Sigma(\vec{\xi}) = \int_{-\infty}^{\infty} \rho(\vec{\xi}, z) dz,$$

where ρ is mass density and z is along the line of sight from the observer to the lens plane. This surface mass density can be made dimensionless, written as κ , by dividing by the critical surface mass density of the universe, which is

$$\Sigma_{crit} = \frac{c^2}{4\pi G} \frac{D_s}{D_d D_{ds}},$$

and

$$\kappa = \frac{\Sigma}{\Sigma_{crit}}.$$

The surface mass density, κ , leads directly to the deflection angle $\vec{\alpha}$ by

$$\vec{\alpha} = \frac{1}{\pi} \int_{\mathbb{R}^2} d^2\theta' \kappa(\vec{\theta}') \frac{\vec{\theta} - \vec{\theta}'}{|\vec{\theta} - \vec{\theta}'|^2}$$

(Schneider, 2003), where $\vec{\theta}$ is the observed angle and is related to the image location by $\vec{\xi} = D_d \vec{\theta}$. This deflection angle $\vec{\alpha}$ can be written as the gradient of a potential ψ , as in $\vec{\alpha} = \vec{\nabla} \psi$, where the potential is defined as

$$\psi = \frac{1}{\pi} \int_{\mathbb{R}^2} d^2\theta' \kappa(\vec{\theta}') \ln |\vec{\theta} - \vec{\theta}'|.$$

There are two primary regimes for gravitational lensing that are important for the study of Abell 2146. Weak lensing occurs in regions where the mass distribution is slowly changing, typically the outskirts of galaxy clusters. The observational effect of weak lensing is that background galaxies will experience slight distortions to their shapes in the forms of magnification and shearing. Since a background galaxy is typically not a perfect sphere, even without a lens, a background galaxy will look like an ellipse. Because of this, a statistical approach has to be taken. Since a galaxy can have a random orientation and shape in the sky before being lensed, we must consider groups of galaxies in small regions such that the average of the random orientations are zero. The size of the region chosen at any particular spot in the field of view depends on the number density of background galaxies. The number of galaxies used in such regions is chosen such that there is a statistically significant signal to noise ratio. For more details regarding weak lensing, see King et al. (2016) for details. This reduces the resolution of weak lensing depending on how large of an area one must use for acquiring a significant signal to noise ratio.

Strong lensing is more sensitive to the inner regions of galaxy clusters. Strong lensing occurs when an image is highly distorted or multiple images of the same background object appear in the sky. Multiple images occur when different points on the lens plane map to the same location in the source plane. The difference between lens types are quantified by κ . A strong lens is the regime for $\kappa > 1$. The case for $\kappa \ll 1$ gives a weak lens.

The basic premise behind a strong lensing analysis in my research is to consider an analytic parametrized description of a mass distribution. The parameters of the profile are constrained by identifying various sets of strongly lensed multiply imaged galaxies.

Here our aim is to determine the centroid of the dark matter in Abell 2146-A in order to establish the spatial location with respect to the X-ray cool core, and hence whether it lags behind the X-ray cool core in their trajectories. We concentrate on modeling the mass around Abell 2146-A using newly-identified multiple image systems to construct the first strong lensing mass model of the system. Strong lensing analysis offers a higher resolution view of the mass around the BCG than obtained with weak lensing. In order to construct the strong lensing mass model we identify new candidate multiple image systems on *HST* images, see Figures 4.1 and 4.3, on the basis of colors and morphologies. Since we do not have spectroscopic or accurate photometric redshift (see equation 1.2) estimates for the candidate multiple images, we adopt a very conservative approach in our threshold for using a candidate system as a constraint.

4.3 Observations and Data Reduction

The merging cluster Abell 2146 was observed with the *Hubble Space Telescope* (HST) on 2013 June 3 and June 6 (HST Cycle 20 proposal 12871, PI:King). A total of 8 orbits of imaging data was obtained with the ACS/WFC camera. There were two pointings in each of the f435W and f606W filters, and four pointings in the f814W filter. The pixel scale of

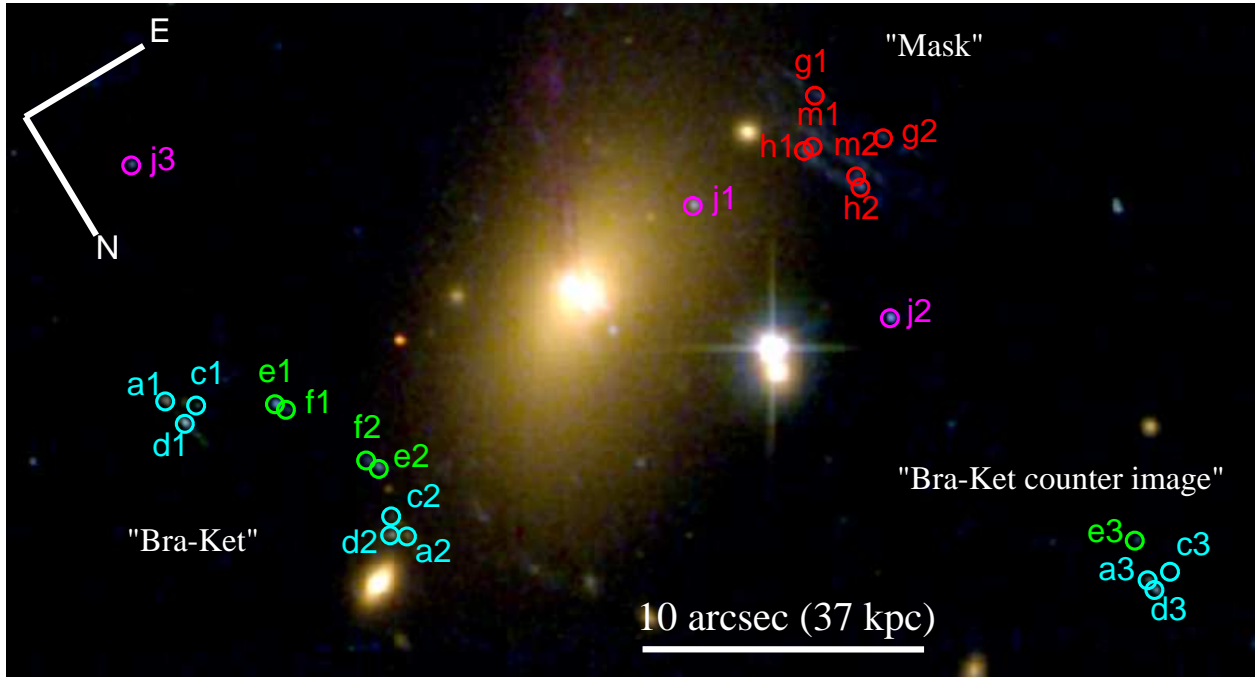


Figure 4.3. Note the rotation; north is towards the bottom right and east is towards the top right. Multiple image systems used as constraints in the vicinity of BCG-A. Identical objects have the same letter prefix, e.g. ‘a1,’ ‘a2,’ and ‘a3.’ The color grouping indicates the objects considered to be at the same redshift. Objects ‘a,’ ‘c,’ and ‘d’ are in cyan. Objects ‘e’ and ‘f’ are in green. Object ‘j’ is in magenta. Objects ‘g,’ ‘h,’ and ‘m’ are in red. The set a, c, and d was statically assigned a redshift of $z = 2.0$. Other systems were assumed to have a flat prior for the redshift in the range $z = 0.3$ to $z = 3.0$.

the images is ~ 0.05 arcseconds. The reduced FITS² files were the same as those used for the weak lensing analysis by King et al. (2016) which should be referred to for additional details. A catalog of objects was created with the freely available software SExtractor (Bertin and Arnouts, 1996).

The position of BCG-A is the barycenter position as calculated by SExtractor (Bertin and Arnouts, 1996). This location corresponds to the peak in the f814W filter within an error of 1 pixel. The full width half maximum of BCG-A in the f814W and f606W filters is on the order of 7 pixels or 3.5 arcseconds.

²‘FITS’ stands for Flexible Image Transport System and is a standard astronomical data format.

4.4 Lens Models

The freely available software LENSTOOL³ (Kneib et al. 1996, Jullo et al. 2007), version 6.8, was used for modeling Abell 2146. LENSTOOL uses Bayesian statistics combined with Markov Chain Monte Carlo techniques to fit a parametrized⁴ lens mass model to gravitational lensing data. Cluster scale mass density profiles, described later, were used to model dark matter components. These density profiles have various parameters that define them, detailed below, and to which some prior is applied. LENSTOOL version 6.8 supports either flat or Gaussian priors on model parameters. Galaxy scale halos were modeled as perturbers to the cluster scale halo, with the perturbers identified in Figure 4.4. The two BCGs were also modeled as perturbers. Typically, they all have the same type of density profile and have certain parameters scaled collectively, as detailed below.

The dark matter halos of Abell 2146 were modeled using a Navarro, Frenk, and White mass density profile (Navarro, Frenk, and White, 1996, hereafter NFW). To allow for departure from spherical symmetry, we used the elliptical NFW mass profile implemented in LENSTOOL (Golse & Kneib 2002). Any mention of a NFW profile should be interpreted as the elliptical NFW profile. Individual galaxies in the cluster are modeled together as a set of perturbers to the cluster scale NFW halo. Collectively the perturbers were modeled as pseudo-isothermal elliptical mass distributions, (Limousin et al. 2007, Elíasdóttir et al. 2007⁵), hereafter PIEMD.

The parameters used to describe the NFW profile are position (x, y) , ellipticity $\epsilon = (a^2 - b^2)/(a^2 + b^2)$ of the projected mass where a and b are the semi-major and semi-minor axes describing the elliptical isodensity contours, θ which describes the orientation angle of

³<http://projets.lam.fr/projects/lenstool/wiki>

⁴Also known as ‘Light Traces Matter’ or LTM.

⁵In Elíasdóttir et al. 2007, the profile is referred to as dual Pseudo Isothermal Elliptical Mass Distribution.

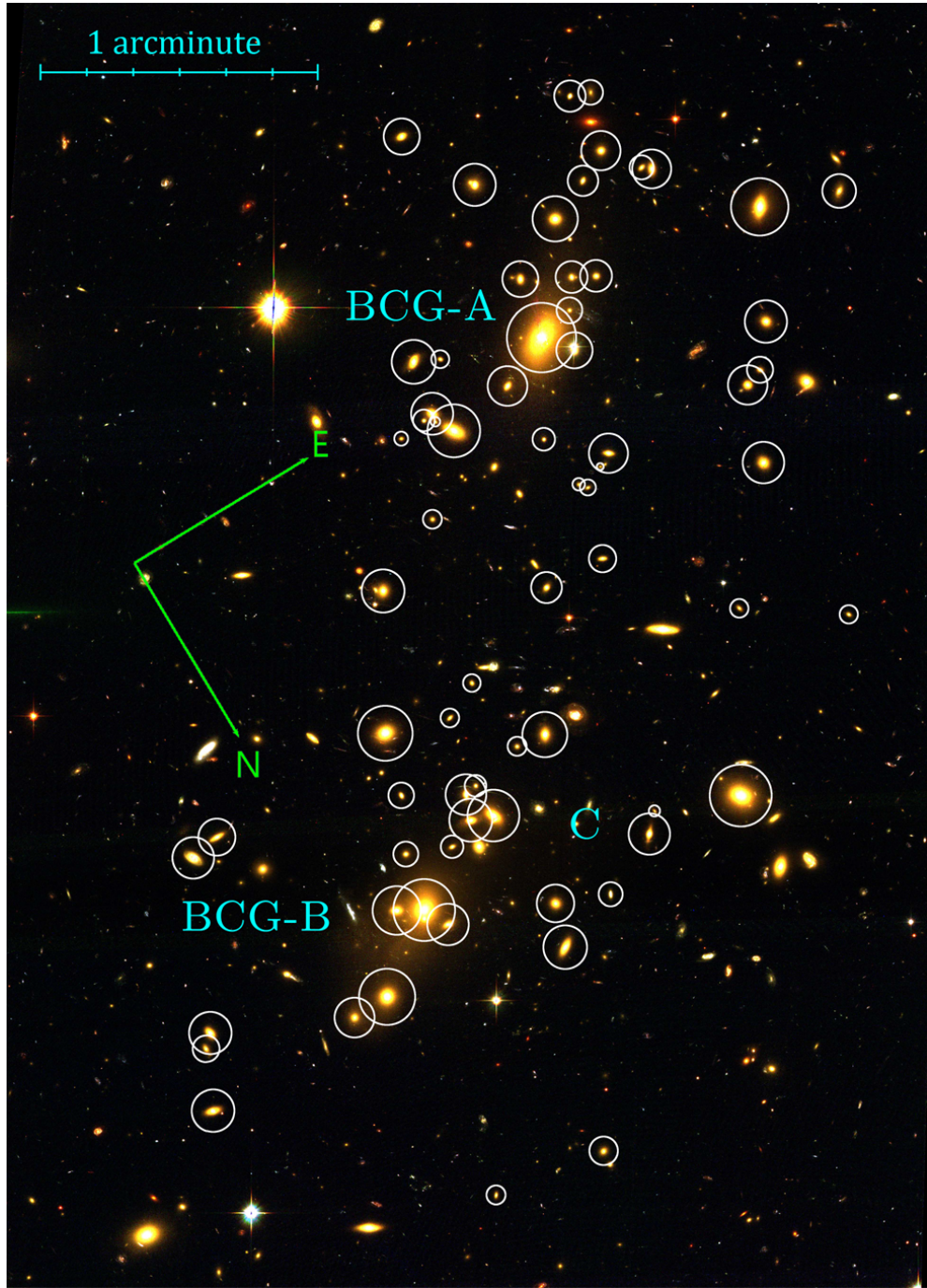


Figure 4.4. A false color picture of Abell 2146. The f814W filter was mapped to the color red, f606W filter was mapped to green, and f435W was mapped to blue. The circles indicate cluster members that are modeled as Pseudo Isothermal Elliptical Mass Distribution (PIEMD) perturbers. BCG-A and BCG-B indicate the brightest cluster galaxies in each of the respective clusters. The location of point C is where a mass overdensity appears in the weak lensing analysis (King et al., 2016). Circle size has no meaning.

the ellipse, and NFW-specific parameters of mass concentration c and scale radius R_s . With the concentration and scale radius related by $cR_s = R_{200}$, when a mass M_{200} (the mass contained inside the radius R_{200} where the mean density is 200 times the critical density at the redshift of the halo) is specified, this reduces by one the degrees of freedom of the model. The NFW profile is truncated at the virial radius which is assumed to be R_{200} .

The analytic description of the spherical NFW profile is

$$\rho(r) = \frac{\delta_c \rho_{crit}}{r/r_s (1 + r/r_s)^2}, \quad (4.1)$$

where the critical density ρ_{crit} is given by

$$\rho_{crit} = \frac{3H^2(z)}{8\pi G},$$

and δ_c , a dimensionless function of the concentration parameter c , is given by

$$\delta_c = \frac{200}{3} \frac{c^3}{(\ln(1+c) - c/(1+c))}$$

with c the concentration parameter and $H(z)$ the Hubble parameter given in equation 1.2. This profile is converted to an elliptical profile by replacing r with $r\sqrt{1 - \varepsilon \cos(2\theta)}$ where we define ellipticity $\varepsilon = (a^2 - b^2)/(a^2 + b^2)$ with semimajor axis a and semiminor axis b , and θ is some rotation angle.

The PIEMD perturbors are described by position (x, y) , ellipticity ε , angle θ , and three PIEMD-specific parameters, velocity dispersion σ_0 , cut radius r_{cut} , and core radius r_{core} . The parameters σ_0 , r_{cut} , and r_{core} are scaled relative to the parameters of an L^* galaxy at the redshift of the cluster; see Jullo et al. (2007) for details. The values used for an L^* galaxy at the redshift of the cluster are given in Table 4.1. The values for M^* , σ_0^* , r_{cut}^* were adopted from one of the CLASH (Postman et al., 2012) mass models by Zitrin⁶, with his technique explained in Zitrin et al. (2013). Both σ_0^* and r_{cut}^* have Gaussian priors. The core radius r_{core}^* is a fixed parameter, typical of an L^* galaxy.

⁶<http://archive.stsci.edu/missions/hlsp/clash/rxj2129/models/zitrin/nfw/v1/>

Table 4.1. Parameters of an L^* elliptical galaxy used in scaling relations. The parameter m_0^* is apparent magnitude, σ_0^* is velocity dispersion, r_{cut}^* is cut radius, and r_{core}^* is core radius. The core radius is a fixed value.

m_0^*	18.070
σ_0^* ($km.s^{-1}$)	99.2 ± 80.0
r_{cut}^* (kpc)	49.3 ± 43.0
r_{core}^* (kpc)	[0.15]

As a consistency check, additional models were created with the software package GLAFIC (Oguri, 2010) as further discussed in the Results and Discussion § 4.8. Optimization of lens models with GLAFIC used a downhill simplex method (Press et al., 1992). As was done with LENSTOOL, the cluster scale dark matter components were modeled with elliptical NFW profiles. The galaxy components were modeled collectively as perturbers consisting of pseudo-Jaffe ellipsoids (Jaffe, 1983; Keeton, 2001). In GLAFIC, the ellipticity used is $\epsilon = 1 - b/a$, where a and b are the semimajor and semiminor axes respectively.

Models in LENSTOOL and GLAFIC had the same constraints and free parameters.

4.5 Procedure

4.5.1 Cluster Member Selection

The cluster members act only as perturbers in the lens model. Their impact is more pronounced when near critical curves. Perturbers were selected from the red cluster sequence of a color-magnitude diagram, as shown in Figure 4.5, and confirmed with visual inspection of the *HST* images that the perturbers were galaxies and not local stars or noise. The perturbers were required to lie on the red sequence in both of the color-magnitude diagrams. A majority of these galaxies have spectroscopic redshifts that were used to establish cluster membership where available (White et al., 2015).

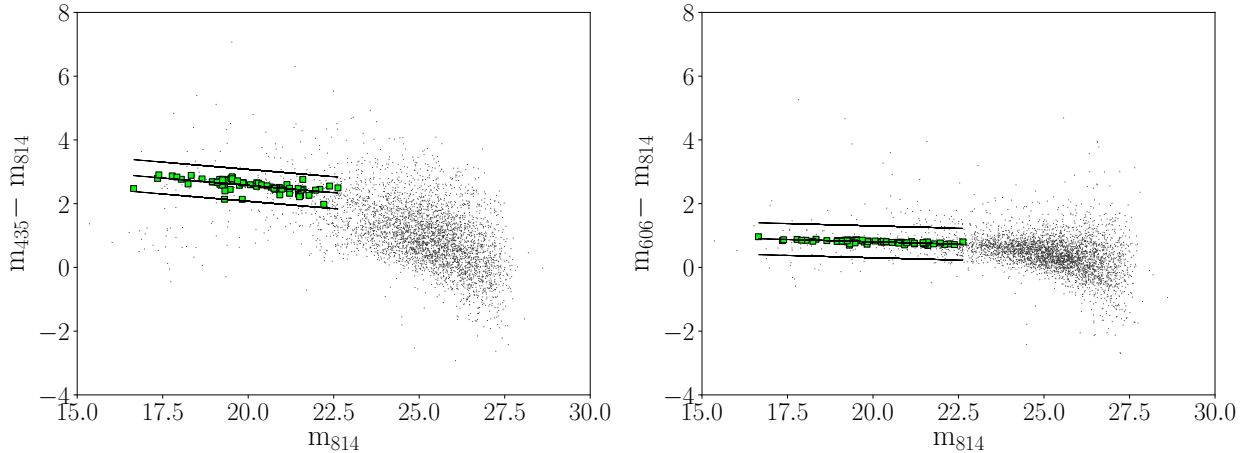


Figure 4.5. Perturbers to the lens model are plotted as green squares; all other galaxies are plotted as points. On the vertical, axis color is computed from SEXTRACTOR (Bertin and Arnouts, 1996) aperture magnitudes, 40 pixel diameter. The horizontal axis is SEXTRACTOR auto magnitudes. Magnitudes are computed from *HST* images. A trend line is plotted through the perturbers with additional lines above and below to show ± 0.5 shift in color of the trend line All of the perturbers are on the red sequence for the cluster.

4.5.2 Model Refinement

Strongly lensed objects are used for constraining a parametric lens model. Of the morphology of a multiple image system, only the positions of the images in the lens plane are used in this paper. The error assumed on the positions of images was 0.3 arcsec to account for telescope resolution as well as substructure in the lens (Massey et al., 2015).

The lens model was iteratively built, starting first with obvious multiple image systems, Figures 4.6 and 4.7. A model was then used to predict and identify other multiply imaged objects. This technique is described in more detail in § 4.5.3.

For extended, irregular background objects, such as an irregular galaxy or merging galaxies, concentrations of baryonic matter can appear as nodules. The positions of the nodules were used as constraints in the lens model (see for example Sharon et al., 2014). For these nodules, the location of the brightest pixel was used as a constraint with an assumed error of 0.3 arcsec or 6 pixels in the *HST* images. For isolated elliptical galaxies, the brightest pixel was used to identify the position of the object.

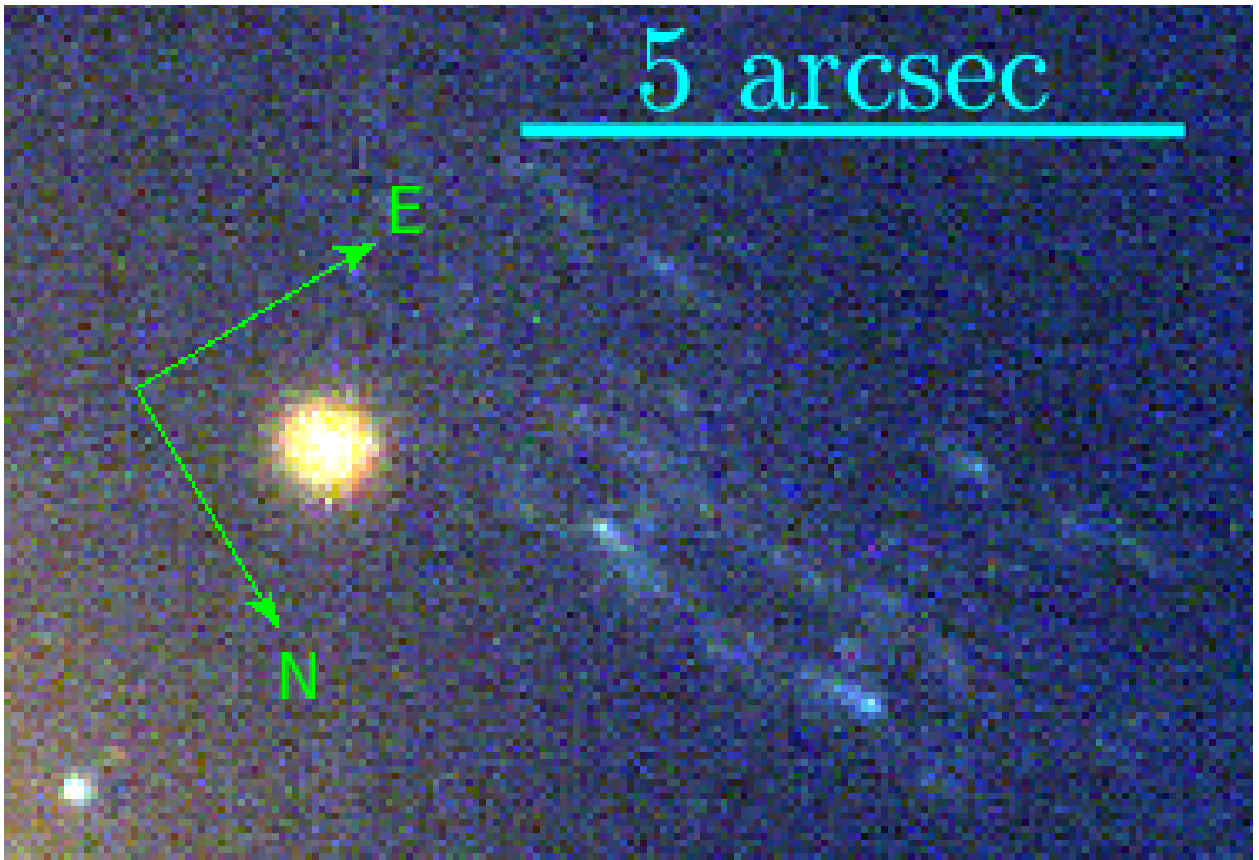


Figure 4.6. Close-up view of a false color image of the ‘mask.’ This system is east of BCG-A. This feature exhibits a bilateral symmetry.

For families of multiple images arising from the same source, the redshift of each of the images was constrained to be identical.

4.5.3 Multiple Image Detection

The following iterative approach was used to predict multiple images. Objects near a Brightest Cluster Galaxy (BCG) are considered to be within the Einstein radius and should be multiply imaged if far enough behind the lens. With a candidate image of a source identified, LENSTOOL was used to predict corresponding counter images for the source, for different source redshifts. With a point in the image plane, a lens model was used to deproject that point onto the source plane at an array of different redshifts. These deprojected points were

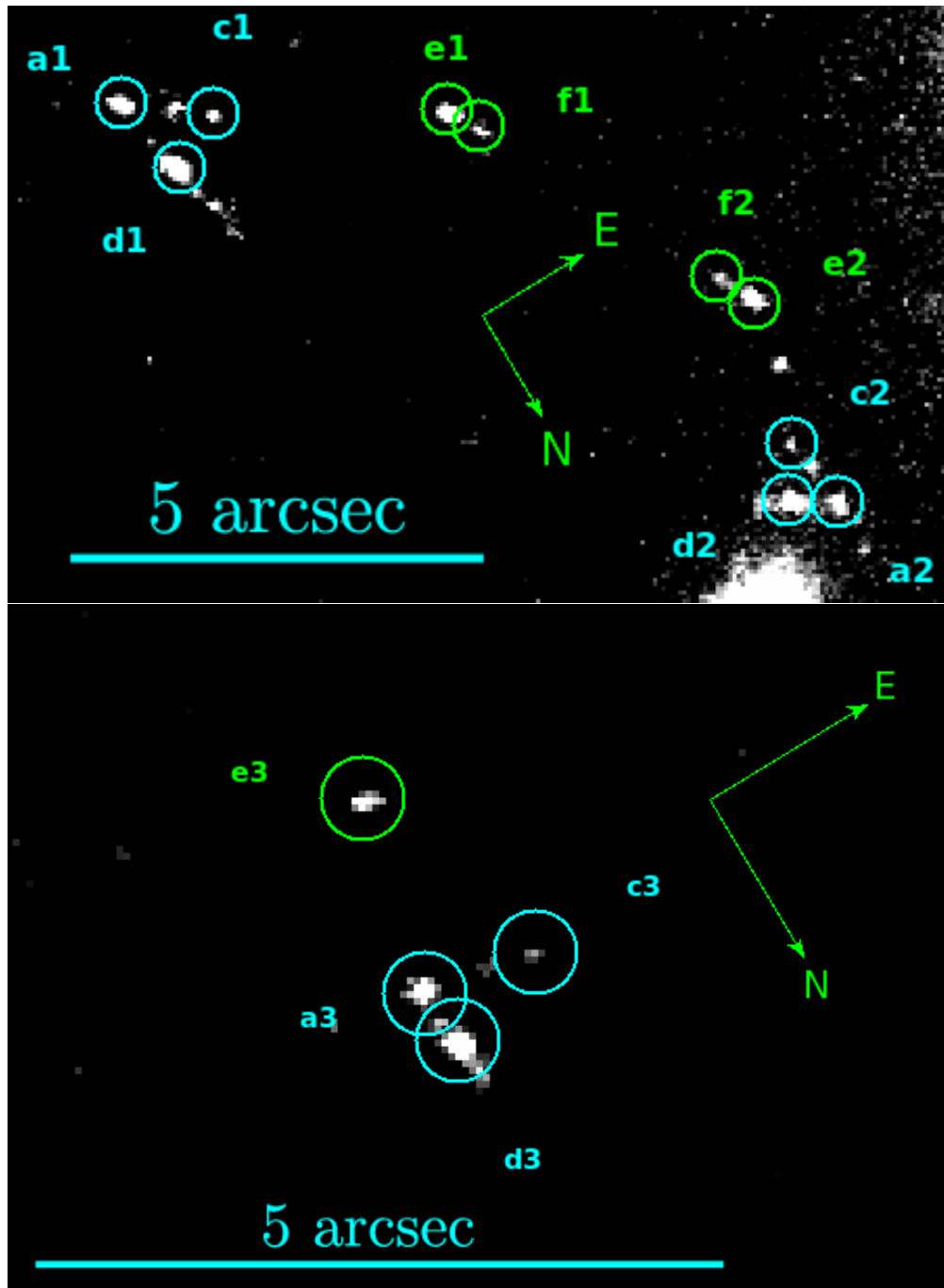


Figure 4.7. From the f606W filter, a close-up view of a high contrast image of the ‘bra-ket’ images, called so because the shape resembles ‘<’ and ‘>.’ In the top panel, the bilateral symmetry is evident and in the bottom panel there is a 3rd counter image. The symmetric pair is located west of BCG-A and the third counter image is northeast of BCG-A. The ‘bra-ket’ system is modeled with points a , c , and d . The blue pair next to ‘<’ and ‘>’ is modeled with points e and f .

then reprojected with the lens model onto the lens plane. Such parametrized-redshift counter images trace one or more lines in the image plane. In Figure 4.8 an object near BCG-A, designated group G1, was tested. The source redshift was parametrized in increments of 0.2 starting at $z = 0.3$ and ending at $z = 2.9$. We limit the range for which we explore the redshift of strongly lensed objects to an upper bound of $z = 3$ because higher redshift objects will be fainter compared with the multiple image systems of interest, and will also drop out of the bluest filter. The graduations in the parametrization of z is arbitrary. The step size of 0.2 used here is for illustrative purposes only. Smaller step sizes were used, on the order of 0.1.

As can be seen in Figure 4.8, the groups of predicted counter images form lines in the image plane. The mass model used to compute this was an intermediate iteration utilizing a subset of the finalized image constraints. The image multiplicity is dependent on the redshift of the lensed object since the caustic structure changes as a function of redshift. Group G2 contains counter images which first appear at source redshift $z = 0.9$. There are no predicted counter images for source redshift $z = 0.3, 0.5, \text{ or } 0.7$ in group G2. In group G3, there were counter images starting at source redshift $z = 0.7$. In groups G4 and G5, counter images started to appear at source redshift $z = 1.7$.

Objects near the predicted counter image line were considered candidates for a multiply imaged system. Color and morphology were taken into consideration. For the lensed source depicted in Figure 4.8, images appeared on both of the lines in groups G2 and G3 near $z = 1.3$, see Figure 4.9. No objects were found on the lines defined by groups G4 and G5. If the test object were to be a member of a multiple image system near redshift $z = 1.3$, then there should be no counter image in groups G4 and G5 since images of those groups do not occur for objects near redshift $z = 1.3$. The three objects taken as a triplet are all blue and are of comparable brightness, and so was considered to be a multiply imaged source.

Multiply imaged objects were added to the model as a further refinement. This second procedure was iterated such that a refined model with extra constraints was used to make

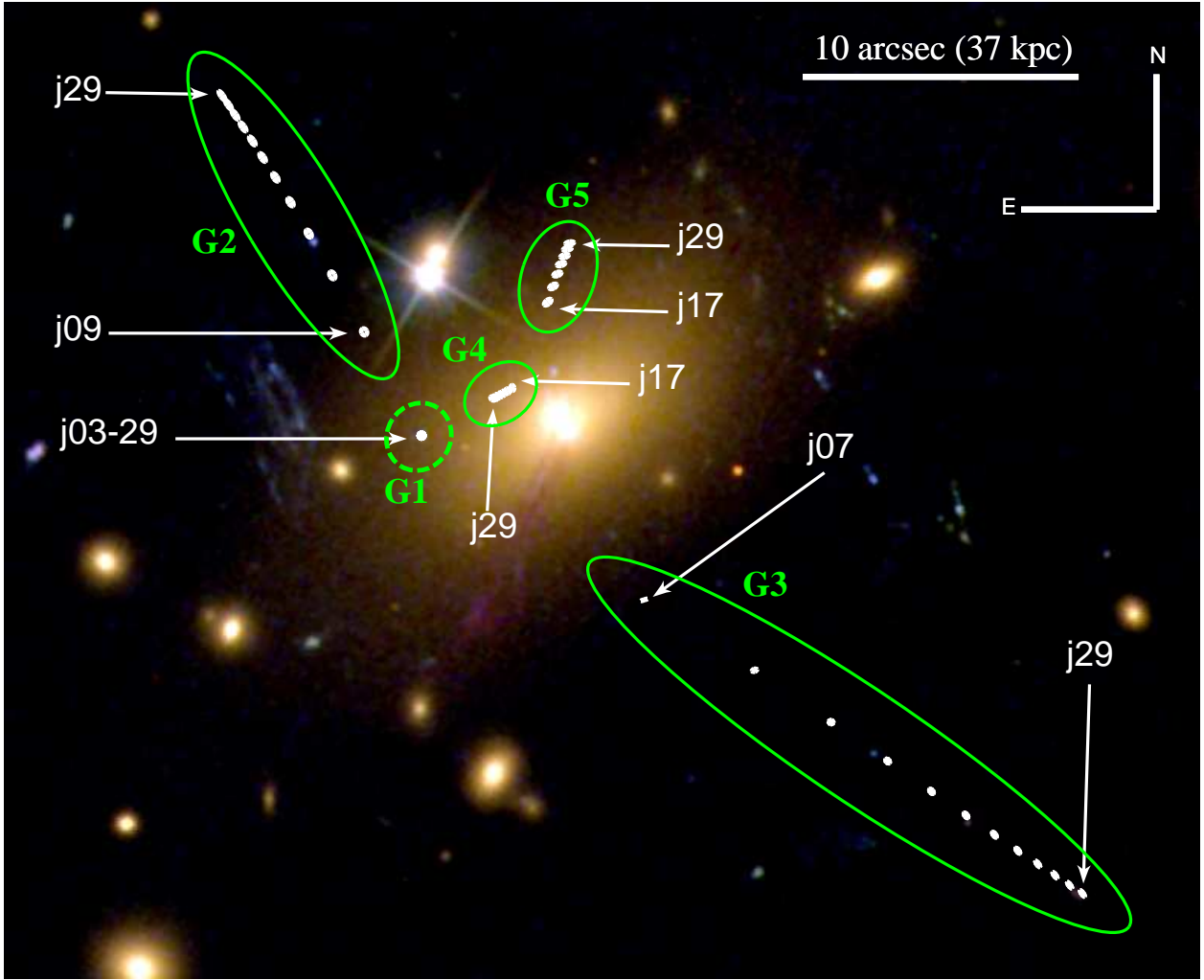


Figure 4.8. In the vicinity of BCG-A, group G1 is the test point in the image plane. Groups G2 through G5 are counter images of G1 parametrized by redshift. The position of an image, G1, is projected from the image plane to the source plane at varying redshifts. The resulting source plane positions of G1 at varying redshifts are then projected onto the lens plane. The multiplicity of an image is dependent on redshift. This results in various predictions of multiple images in groups G2 through G5 as functions of assumed redshift of the source of the image in group G1. Group G2 begins at a redshift of $z = 0.9$, group G3 begins at $z = 0.7$, and groups G4 and G5 begin to appear at a redshift of $z = 1.7$.

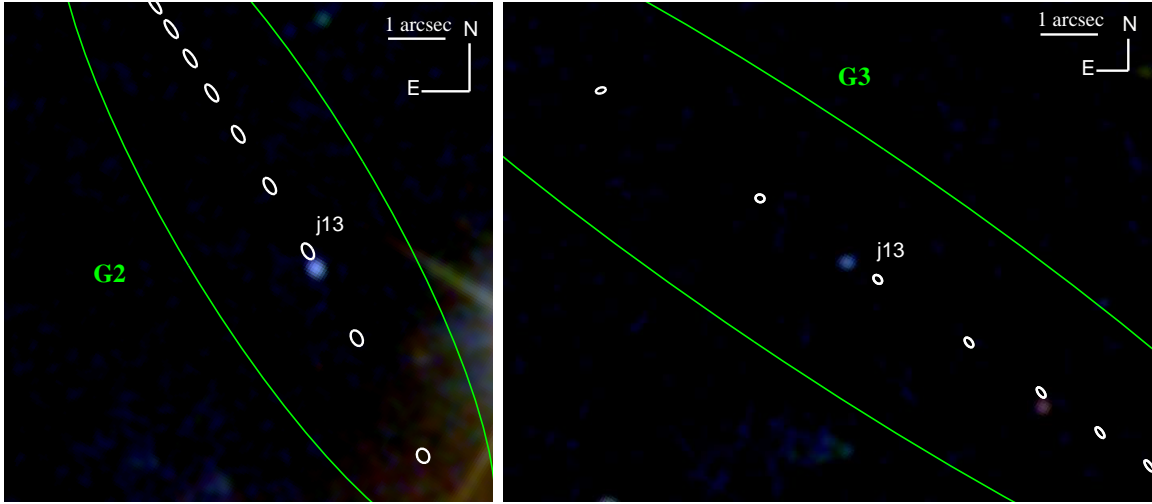


Figure 4.9. In the left frame, an expanded view of the region around G2 in Figure 4.8. There is a blue galaxy as a possible counter image for some assumed redshift of G1 slightly less than $Z = 1.3$ for some intermediate mass model. The counter images in this group have an increasing redshift in the northeast direction. In the right frame, a blue galaxy in group G3 appears as a possible counter image for the same assumed redshift of G1 between the same range of redshifts as the galaxy in the left frame. Both of these galaxies are on the redshift parametrized path at the same z location.

further predictions for additional possible multiple image systems. Predicted multiple image systems that worsened the best fit of the lens model were discarded.

4.6 Lens Model Constraints

Multiple image systems were used as constraints and are presented here. In the refinement state of generating lens models, more systems were used than are presented here. Specifically, the multiple image systems and arcs around the second brightest cluster galaxy, BCG-B, were not used in the final models presented here, but were used in the intermediate stages for some variations to explore parameter space and to test convergence of the models.

There are four main groups of multiple image systems near BCG-A. An object is denoted by a letter followed by a unique ordinal, where objects with the same first letter are considered

to belong to the same multiple image system. In Figure 4.3, corresponding lensed images considered to be at the same redshift are denoted with the same colors.

4.7 Computation

For LENSTOOL, optimization was performed in the source plane in the refinement stage of the lens model construction where various multiple image systems were considered. Optimization is done with Markov Chain Monte Carlo (MCMC) such that the locations of all projected of all components of a multiple imaged object should have their projected separation distances minimized. Final models were optimized in the image plane where for each item in a multiple image system, the location gets projected from the lens plane to the source plane, then that location is reprojected back into the lens plane to create a set of multiple positions. One thousand samples were taken for each of the image plane optimized models. For optimization in the source plane, the χ^2 fit uses the computed source positions relative to the barycenter of the multiple images in the source plane (Jullo et al., 2007). The image plane optimization is more computationally expensive as the χ^2 minimization must solve the lens equation to find counter images in the lens plane (Jullo et al., 2007). The χ^2 contribution for lens plane optimization, equation 9 in Jullo et al. (2007), is for some source i

$$\chi_i^2 = \sum_{j=1}^{n_i} \frac{[x_{obs}^j - x^j(\vec{\theta})]^2}{\sigma_{ij}^2}, \quad (4.2)$$

where n_i is the number of multiple images for i , x_{obs}^j is the observed location, $x^j(\theta)$ is the position predicted by the model, $\vec{\theta}$ is the array of model parameters, and σ_{ij}^2 is the error of the position of j , which is assumed to be 0.3 arcseconds. The χ^2 value is used as a parameter in the likelihood function (Jullo et al., 2007).

The so-called Rate parameter, as defined in Jullo et al. (2007, see eq. 13), was set to 0.1. This parameter controls the speed at which the modeling converges. The value used for the

Rate is on the lower end of the range suggested in Jullo et al. (2007). Larger values for the final lens models did not alter the main results of this paper.

For GLAFIC, optimization was performed in the source plane but with the full magnification tensor to convert offsets in the source plane to those in the image plane. It has been shown that the resulting χ^2 computed in the source plane accurately reproduces χ^2 directly computed in the image plane (Oguri, 2010).

4.8 Results and Discussion

In this section the results are presented for several image plane optimized models. In all models the ‘bra-ket’ system, composed of objects ‘a,’ ‘c,’ and ‘d,’ shaped like ‘<’ and ‘>’, Figures 4.3 and 4.7, was statically assigned a redshift of $z = 2.0$. This designation was used to break a degeneracy between the redshift of the multiply lensed objects and the mass of the lens. We expect that images would drop out of the f435W filter near a redshift of $z = 3.0$. The models explored a flat prior on source redshift for each of the multiple image systems over a range of redshift from $z = 0.3$, which is just beyond the cluster redshift, to $z = 3.0$. Other values for the redshift at which the bra-ket system was statically assigned were explored and had no impact on the conclusions regarding the location of the dark matter halo A.

The convergence κ , or dimensionless surface mass density (Schneider et al., 1995), of the lens is a function of source redshift due to the dependence on the critical surface mass density $\Sigma_{crit} = c^2 D_S / (4\pi G D_L D_{LS})$ where D_S , D_L , and D_{LS} are the source, lens, and lens-source angular diameter distances respectively. In this paper we are concerned with the centroid of the mass, which is rather insensitive to the redshifts of the lensed sources adopted. We have established this by using different assigned redshifts in the lens modeling. Lack of knowledge of the source redshifts does have an impact on the normalization of the mass profile, and the determination of the total mass. In any case, the choice of $z = 2.0$ for a static redshift

for the ‘bra-ket’ multiple image system does not significantly alter the mass. The variation in mass was less than an order of magnitude. For example, comparing the convergence for a source at redshift $z = 1.0$ and at $z = 2.0$ we obtain

$$\kappa_{z=1} = \left(\frac{\Sigma_{crit,z=2}}{\Sigma_{crit,z=1}} \right) \kappa_{z=2} = (0.86) \kappa_{z=2}, \quad (4.3)$$

which shows that the particular choice of redshift for one of the sources does not appreciably change the mass.

The choice of a redshift for a source image is to break a degeneracy for the mass of the halo and is arbitrarily chosen to be within the range of redshift of the cluster at $z = 0.2323$ and $z = 3.0$, where the upper bound of $z = 3.0$ is where we expect dropouts to occur for given *HST* filters used in this study. The degeneracy is evident from equation 4.3 where, for some projected surface mass density Σ , we have $\Sigma = \kappa \Sigma_{crit}$ (Schneider et al., 1995). With the redshift of the lens known, the term Σ_{crit} is a function of the redshift of the source. From the geometry of the source images we determine κ . However, κ is a ratio of the mass of the lens via the projected surface density Σ and Σ_{crit} , which are both unknown. This gives a degeneracy between mass of the lens and the redshift of the sources.

For NFW profiles the concentrations were also held fixed. We expected the turnover radius to be well beyond the field of view of the *HST* images. With no information to constrain this radius since strong lensing features are typically only found in a relatively small area, the solution is simply to hold the scale radius, r_s , to be fixed and allow the concentration to be a free parameter. However, in this paper the concentration was fixed and the scale radius was a free parameter. Both parameters are related by $cr_s = r_{200}$. Holding c fixed with r_s free is the same as having c free and r_s fixed.

We found that the position of the dark matter halo associated with Abell 2146-B was not well constrained. This lack of constraint was due to, in part, the presence of many massive galaxies close to the BCG contributing to strong lensing, and more importantly, a

lack of redshift information or clear corresponding morphological features for arcs to identify corresponding multiple images.

The following are examples of candidate multiple image systems that were used in order to try to constrain the mass distribution of Abell 2146-B: (i) There is a large arc near BCG-B which was used as a constraint, however it is near to a group of 4 galaxies that are perturbing the shape of the arc. (ii) There is also a faint blue feature in the stellar halo of BCG-B that appears to be a multiple image system. (iii) Additionally, east of BCG-B there is an elongated arc that looks multiply imaged. This object is likely to be relatively high redshift since it drops out of the f435W and f606W filters. However, it is detected at a low signal to noise ratio in f814W, so the detection threshold in the other filters have to be accounted for in future studies of Abell 2146-B.

The refinement technique described in § 4.5.2 for predicting multiple image systems yielded unsatisfactory models. An unsatisfactory model is one where the model fails to converge for one or more parameters. With the model failing to converge on a solution it becomes problematic in sampling from the distribution to create a predictive intermediate model. This may also indicate that the dark matter is disrupted near BCG-B such that the matter distribution is not a smooth NFW profile due to the merger. In early stages of model refinement, the position of the dark matter (DM) halo associated with BCG-B was allowed to vary. However, since the location of DM halo B never converged to an acceptable solution due to lack of multiple image systems as constraints, in later stages of model refinement the DM halo B was set to a static position coincident with BCG-B, and models with two fixed halos to describe Abell 2146-B were also considered.

Since we were not able to constrain the location of DM halo B, the final models presented below have static NFW profiles associated with Abell 2146-B, and the multiple image systems associated with Abell 2146-B are discussed no further. The main science goal was to determine the location of the dark matter halo associated with Abell 2146-A. The static

halos representing Abell 2146-B are far enough away from Abell 2146-A such that the only major effect is to provide some shear and very slightly offset the location of halo A. The shift in position is 1.2 arcsec due to the additional fixed parameter halos.

We present three lens models here designated as model 1, 2, and 3. In all models, there is a dark matter NFW halo associated with Abell 2146-A, halo A. The major distinctions between the models are specified below.

4.8.1 Model 1

This model used only one NFW profile associated with Abell 2146-A. The concentration was held fixed at $c = 3.5$. The other parameters of the NFW profile were free as described earlier. See Table 4.2 for a side by side comparison of fixed parameters between the models.

4.8.2 Model 2

In addition to the NFW halo associated with Abell 2146-A in Model 1, this model had a second dark matter halo placed at the location of BCG-B. This second halo was static in the sense that all parameters, namely M_{200} , c , position, ellipticity, and position angle were fixed. This gives this model a total of two NFW profiles to describe the cluster.

The placement of the second NFW profile assumed that light traces matter. The ellipticity and position angle of BCG-B were used to describe the dark matter (DM) halo, in addition to the location of the DM halo being coincident with the peak of BCG-B.

Mass and concentration parameters of the NFW profile obtained from earlier models were used as a reference for these statically assigned parameters. The mass and concentration was chosen to be consistent with the weak lensing analysis by King et al. (2016) such that they were of the same order. The weak lensing analysis by King et al. (2016) looked at concentrations between 3.5 and 4.5., however intermediate strong lensing models resulted in lower concentrations at around $c = 3.1$. The mass of halo B from intermediate models was

on the order of $10^{14}M_{\odot}$ where a specific choice of $4 \times 10^{14}M_{\odot}$ obtained from an intermediate strong lens model was used in the final models. The scale radius was determined from the assumed mass and concentration.

4.8.3 Model 3

This model has a total of three NFW profiles. The dark matter associated with Abell 2146-B was represented with two NFW profiles. One of the profiles was centered and fixed on the BCG-B, halo B, as was done in Model 2, and the other was fixed at the location of the centroid of a mass peak seen in the weak lensing analysis by King et al. (2016), halo C. See Figure 4.4 for the location of halo C. While the presence of a mass peak at the location of halo C is indicated by the weak lensing analysis (King et al., 2016), there are no obvious strongly lensed features associated with this peak that might allow us to better constrain its properties.

The observed ellipticity and position angle of the BCG-B were used to describe the NFW halo B centered at the same location, i.e. light traces mass. Halo C was assumed to be spherical, since there are no strong constraints from weak or strong lensing.

The total mass of halo B from model 2 was divided equally between halo B and halo C of model 3.

4.8.4 Other Models

Additional models were considered with BCG-B having free parameters constrained by multiple image systems nearby. However, as noted above, these models were unable to converge to a stable solution. Therefore, associated arcs and multiple images near BCG-B were not used for any of models 1, 2, or 3 above.

The associated gas of the cluster was considered as a perturbation in intermediate versions of the lens model in order to establish its significance in the modeling. The impact of the

Table 4.2. Comparison of distinguishing features between lens models 1, 2, and 3. Mass is given in units of $10^{15}M_{\odot}$. All parameters of halo B and halo C are fixed.

	Model 1	Model 2	Model 3
Halo A			
c	3.5	3.5	3.5
Halo B			
ϵ	-	0.177	0.177
PA	-	141.9	141.9
M_{200}	-	0.4148	0.2074
c	-	3.1	3.1
Halo C			
ϵ	-	-	0
PA	-	-	0
M_{200}	-	-	0.2074
c	-	-	3.1

gas was to displace the centroid of the DM halo A away from the gas peak, towards BCG-B. In the final models presented here, we do not include a gas component in the model. The results here are therefore a lower bound on the separation between the dark matter halo and the X-ray cool core, since a gas component at the location of the cool X-ray core only increased the separation.

In Table 4.3, Model 1, which had only one dark matter NFW halo, had a better χ^2 per degree of freedom compared to Model 2 and 3. However, we do expect there to be dark matter near BCG-B as evidenced by the weak lensing analysis (King et al., 2016). Model 2 had the largest $\text{Ln}(\text{Evidence})$ (Trotta, 2008) value relative to Models 1 and 3 which indicates a preference for two dark matter halos when using $\text{Ln}(\text{Evidence})$ to classify goodness of fit of models. By considering the Bayes factor and Jeffrey’s scale from Trotta (2008), computed by exponentiating the difference of the $\text{Ln}(\text{Evidence})$, we can see that Model 3 is weakly preferential to Model 1, and that Model 2 is moderately preferential to either of the other two models.

All models considered, including versions not presented here, resulted in a well constrained centroid for dark matter (DM) halo A. In each model, the DM halo A was coinci-

dent with BCG-A, and thus lagging behind the leading gas peak. In Figure 4.10 there are 1000 samples from the best model obtained from LENSTOOL for Models 1, 2, and 3 which are plotted over the HST image. A 3σ curve is drawn around the samples. All of the final models presented here result in the BCG-A peak being around approximately 3σ of the mean location of the DM halo A. The presence of mass associated with DM halo B or C shift the centroid of halo A away and towards the X-ray peak.

As a consistency check, the strong lensing program GLAFIC (Oguri, 2010) was used to verify model selection. In some instances of models that don't converge to a solution, or when the specified error on image positions, σ_{ij} in equation 4.2, is too small, LENSTOOL will fail to generate a model that can reproduce the input constraints. This is most likely due to source positions being very close to a complicated caustic line. As a measure of the quality of a lens model we expect that solutions for source positions corresponding to image position constraints are properly projected from their corresponding source plane position to the lens plane position which was used as a constraint in constructing the model. In other words, for a given image used to construct a lens model that predicts a source position, we expect to use the lens model and project the source position and recover the image positions used in constructing the model. For LENSTOOL, this can occur in the cases mentioned above. GLAFIC allows for requiring solutions to match the number of aforementioned projected images with the number of images used as constraints in building the lens model. Both of these behaviors are complementary in constructing lens models.

The error and location of DM halo A was consistent with results produced with LENSTOOL. For GLAFIC Models 1, 2, and 3 the separation distances between the dark matter halo centroid and BCG-A are, respectively, 4.52, 2.67, and 5.67 kpc. The GLAFIC Models 1, 2, and 3 separation distances between the dark matter halo and the X-ray peak are, respectively, 28.1, 28.9, and 26.4 kpc. Each respective result from the three GLAFIC models for the DM halo A position was within 3σ for all three LENSTOOL models. That is to say that DM

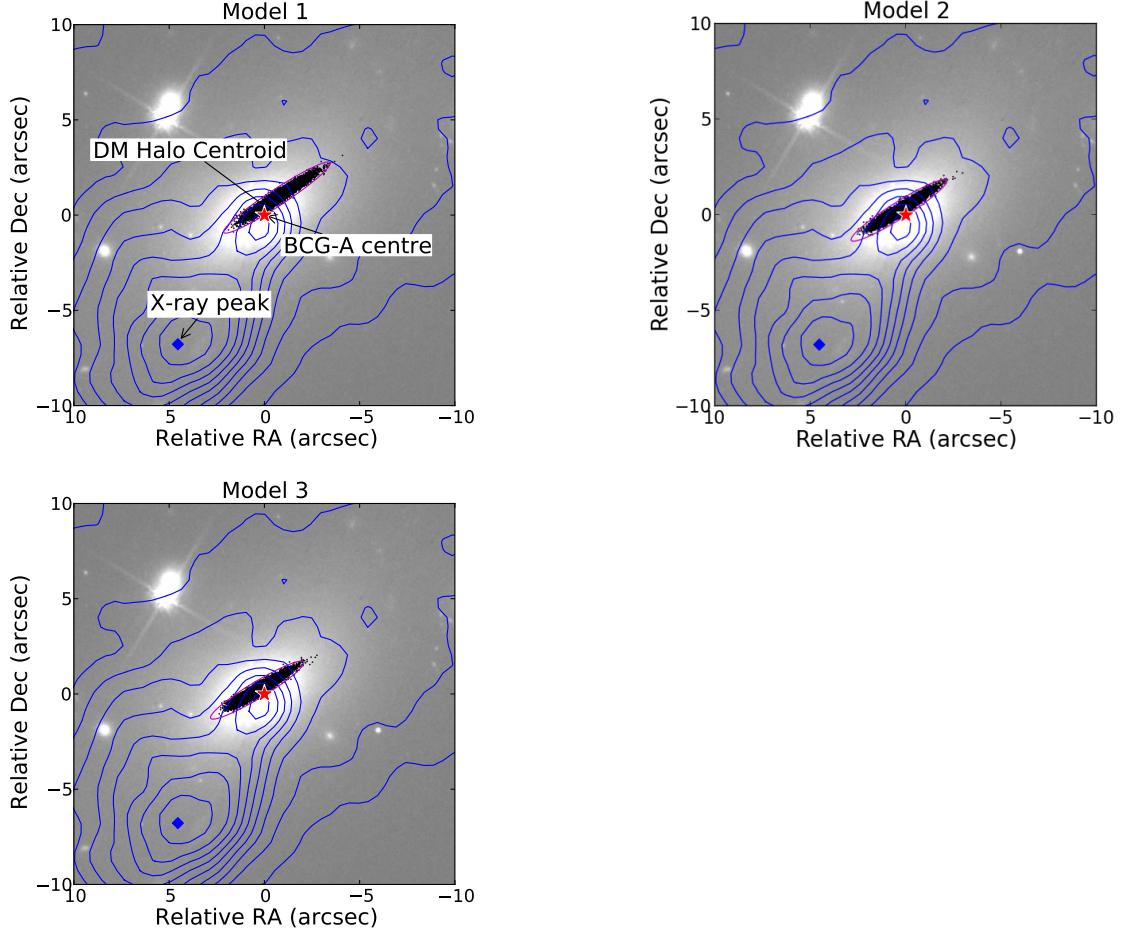


Figure 4.10. The red star is the center of the BCG-A as determined with `SExtractor` and the blue diamond is the peak of the hot X-ray gas (Russell et al., 2010, 2012). The collection of black points near the BCG-A center is a plot of the centroid of dark matter halo for 1000 samples from the best fit lens model. North is up and east is left. Top image is model 1, middle image is model 2, and bottom image is model 3. BCG-B is out of the frame to the northwest (or top right) direction from BCG-A. The contours are from *Chandra X-ray Observatory* with a 3 pixel Gaussian smoothing. Note that the second X-ray peak coincident with BCG-A is a point source associated with the AGN of the BCG. This is not a gas peak. The X-rays from this point source are non-thermal (Russell et al., 2012).

Table 4.3. Comparison of results from lens models 1, 2, and 3. The Mean Position is for the dark matter centroid. The error matrix shows the variance and covariance of the dark matter halo position. The separations are between the mean position of the dark matter centroid and either the peak light position of BCG-A or the X-ray peak. The Ln(Evidence) for Model 2 yields a significant Bayes factor (Trotta, 2008) relative to either of the other models.

	Model 1	Model 2	Model 3
Mean Position (deg)			
RA	239°05789	239°05860	239°05861
Dec	66°348371	66°348183	66°348171
Error Matrix (arcsec)			
σ_{RA}^2	0.7	0.5	0.5
σ_{Dec}^2	0.3	0.2	0.2
$Cov(RA, Dec)$	0.4	0.3	0.3
Separation Distances (kpc)			
BCG-A	4.19	1.63	1.59
X-ray peak	34.5	30.3	30.2
Ln(Evidence)	36.8	41.1	37.8
χ^2/dof	0.51	0.38	0.18

halo A position results from GLAFICModel 1 were within the 3σ boundary for each of the LENSTOOL models, and so forth for each GLAFIC model.

4.9 Conclusion

We have used *Hubble Space Telescope* images to identify strongly lensed multiple image systems near to the BCGs of the merging cluster, Abell 2146. This merging cluster is an important laboratory for studying the physics of cluster mergers because the collision has occurred near the plane of the sky, the two clusters in the system are of comparable mass, and the system also has two well-defined shock fronts. The BCG in Abell 2146-A has an X-ray cool core. By identifying multiple image systems in the center of Abell 2146-A, we have made a strong gravitational lensing mass model. We have determined that the location of the dark matter halo is coincident with the BCG, and is offset from the X-ray cool core. In other words, from this strong lensing analysis, the cool core is leading, rather than lagging,

the dark matter post collision, contrary to expectations for a merger seen shortly after first core passage.

In Canning et al. (2012) it is proposed that there is a causal link between the X-ray cool core and a plume of gas extending from the BCG in its direction, which is spatially coincident with soft X-ray emission. Together with the disrupted nuclear structure of the BCG, an interaction between the BCG and another galaxy in the cluster (prior to or during the merger) is proposed as a possible explanation of the offset between the BCG and the X-ray cool core (Canning et al., 2012).

Hamer et al. (2012) describe three clusters with significant offsets between the BCG and X-ray peak with the conclusion that a transitory event is the source of decoupling. The largest separation distance in Hamer et al. (2012) is on the order of 10 kpc, whereas in Abell 2146, the offset is on the order of 30 kpc.

However, in light of Sanderson et al. (2009), Abell 2146-A seems to fall in the upper range of offsets for BCG with line emission (Crawford et al., 1999).

In order to test these hypotheses and to better understand the distribution of the dark matter (and galaxies), and plasma in the aftermath of the collision, computer simulations are being undertaken. These simulations will be guided by the results of lensing, X-ray, SZ and additional data.

Redshift information for the strongly lensed features is critical to obtaining a properly normalized strong lensing mass model for Abell 2146-A. This redshift information would in addition allow us to identify multiple image systems to use as constraints in mapping the distribution of mass in Abell 2146-B. For objects that are bright enough, spectroscopic redshifts would be ideal, and otherwise photometric redshifts can be obtained with the addition of near-infrared imaging data to complement our optical imaging data. More work needs to be done to constrain the dark matter near BCG-B. A combined weak and strong lensing analysis will help accomplish this.

CHAPTER 5

HYDRODYNAMIC SIMULATIONS OF ABELL 2146

5.1 Introduction

The location of the peak in the X-ray signal was determined to be ahead of the more massive cluster (Coleman et al., 2017; King et al., 2016). Simulations of clusters can have varying levels of complexity depending on the prescription for the physics included in the software that is used to model the system. Abell 2146 is of interest because it is a relatively well behaved merger with properties, such as having a merger axis close to the plane of the sky, that are well documented and, in the case of the X-ray peak location, not well understood.

Here we present a simple hydrodynamic simulation that aims to capture bulk properties of the system, such as how various descriptions of the corresponding halos effect each other. In the weak lensing analysis (King et al., 2016) we can see, that after collision, one of the halos appears disrupted with no cool core of gas. We attempt to reproduce such large scale results with simple models.

The simulations assumed a cosmology with a Hubble constant $H_0 = 70 \text{ km s}^{-1} \text{ Mpc}^{-1}$, with dark energy fraction $\Omega_\Lambda = 0.7$, and baryonic fraction $\Omega_m = 0.3$ in a spatially flat universe.

5.2 Simulation Background and Theory

Dark matter is treated as a collisionless fluid that obeys the collisionless Boltzmann equation which is

$$\frac{df}{dt} = 0, \tag{5.1}$$

where $f = f(\mathbf{x}, \mathbf{v}, t)$ is the distribution function of the system in phase space. To account for forces on the particles, Poisson's equation,

$$\nabla^2 \Phi = 4\pi G\rho, \tag{5.2}$$

is used with equation 5.1, where Φ is the potential, G is Newton’s gravitational constant, and ρ is the density. By expanding the total derivative in equation 5.1, one gets

$$\frac{\partial f}{\partial t} + \frac{\partial \mathbf{x}}{\partial t} \frac{\partial f}{\partial \mathbf{x}} + \frac{\partial \mathbf{v}}{\partial t} \frac{\partial f}{\partial \mathbf{v}} = 0 \quad (5.3)$$

which can be rewritten using $\frac{\partial \mathbf{x}}{\partial t} = \mathbf{v}$ and $-\nabla \phi = \frac{\partial \mathbf{v}}{\partial t}$ as

$$\frac{\partial f}{\partial t} + \mathbf{v} \frac{\partial f}{\partial \mathbf{x}} - \nabla \phi \frac{\partial f}{\partial \mathbf{v}} = 0. \quad (5.4)$$

Many options are available for performing hydrodynamic simulations in astrophysics, such as RAMSES (Teyssier, 2002), AREPO (Springel, 2010a), ENZO (Bryan et al., 2014) or GADGET-2 (Springel et al., 2001; Springel, 2005). Of the differences in the software codes, some are publicly available while others are either private or require explicit permission from the author. Other differences include the mathematical formalism for computing hydrodynamic solutions and, additionally, differences in implemented physics.

The two major classes of hydrodynamic solvers are Eulerian or Lagrangian. The Eulerian approach is a grid approach that approximates a continuous volume. The volume elements of the grid need not be identical in size and can also be adaptive (Teyssier, 2002). Each volume element of space has, at the very least, some density and pressure. The density and pressure of a volume element changes by the flow of fluid in and out of the element. In the grid representation, the idealized continuous functions of pressure and density are discretized according to the grid decomposition of space. More advanced physics can attribute more properties, such as charge or magnetic field, for these volume elements. In the Lagrangian formalism the sampling coordinates are co-moving with regard to the velocity flow of the fluid. The grid is represented by “particles” that are weighted by mass. In regions of high density a simulation will have more grid points from which to sample the properties of the fluid. These techniques can be combined (Hirt et al., 1974) with the caveat that any problems with either system are combined as well, such as issues handling vortices where a

mesh can get entangled, or oscillation instabilities when momentum diffusion lengths do not match with cell sizes. There are modern codes that combine the Lagrangian and Eulerian techniques in different ways that can overcome these issues (Springel, 2010a).

The public and well tested software GADGET-2 (Springel et al., 2001; Springel, 2005) was used for hydrodynamical simulations of Abell 2146. GADGET-2 is a Lagrangian or smooth particle hydrodynamics (SPH) N-body solver. Various software was considered and tested, however GADGET-2 was chosen for speed, robustness and documentation. Recent reviews of smooth particle hydrodynamics are (Price, 2005) and (Rosswog, 2009), with details about more modern techniques given by Springel (2010b) and Cossins (2010).

5.3 Initial Conditions

The initial conditions for the hydrodynamical simulation of Abell 2146 consisted of mass particles representing idealized galaxy clusters constituted of a combination of dark matter and baryonic matter. The baryonic component represented the intracluster medium, which is an ionized gas of mostly Hydrogen and Helium. For each cluster, it is assumed that the gas is in hydrostatic equilibrium.

Also required of the initial conditions is that the density profiles are stable. This is to say we required for a single halo the ability of the halo to maintain the given density distribution over the course of a time scale sufficient for collisions to occur. Halo stability allowed for the determination that the hydrodynamic software was working correctly, and also allowed for reproducibility of starting conditions for comparison with other research.

5.3.1 Hernquist Density Profile

Both dark matter and gas were represented with a Hernquist density profile (Hernquist, 1990; Springel et al., 2005; Robertson et al., 2017) due to it having an analytic distribution function and also being finite in mass. In large scale cosmological simulations where a homogeneous

distribution of matter is allowed to form structure through gravitational collapse, the NFW density profile (Equation 4.1) is found to be an average representation of the collapsed matter (Navarro et al., 1996). The profile appears in these simulations for any assumed values of the dark matter and dark energy in the simulation, and for this reason the NFW profile is “universal.” However, the NFW profile has infinite mass which requires, for its use in simulations, some truncation at some finite distance from the core. This truncation can cause issues with stability unless handled properly, such as with some smoothing function that tends to zero at some finite radius.

The Hernquist density profile is

$$\rho(r) = \frac{M a}{2\pi r} \frac{1}{(r + a)^3}, \quad (5.5)$$

where M is the total mass, r the radius, and a is a scaling factor. The Hernquist profile is determined with two free parameters, M and a . For comparison with literature that use the NFW profile, which is also determined with two parameters, we allowed for matching the Hernquist parameters to NFW parameters. Springel et al. (2005) used a similar approach, but made a different choice on how to match certain parameters. However, the technique used for matching parameters between NFW and Hernquist profiles was adapted from Robertson et al. (2017).

For NFW profiles, the mass specified is often M_{200} , which is the mass contained in a radius R_{200} such that the density in the volume is 200 times the critical density of the universe at some specified redshift. As mentioned in Chapter 4, but reproduced here for convenience, we have

$$M_{200} = \left(\frac{4}{3} \pi R_{200}^3 \right) 200 \rho_{crit}, \quad (5.6)$$

where the ρ_{crit} is the critical density. Given the mass M_{200} , equation 5.6 can be solved for R_{200} . The mass M_{200} was used for both NFW and Hernquist profiles. The remaining parameters are the scale length a in Hernquist and concentration c in NFW.

For the Hernquist density, the mass enclosed inside some radius r is given by

$$M(r) = M \frac{r^2}{(r + a)^2}, \quad (5.7)$$

where M is the total finite mass in a Hernquist profile. Here, we required the mass enclosed inside R_{200} to be M_{200} . Springel et al. (2005) requires that the total mass be M_{200} , and this causes a difference in how the NFW concentration parameter c relates to the Hernquist scale factor a . In Figure 5.1, an NFW profile is plotted for a halo with mass $M_{200} = 1.1 \times 10^{15} M_{\odot}$ and concentration $c = 3.5$ radially from 10 kpc up to R_{200} , where two Hernquist parameter matching schemes are compared. When stipulating the total Hernquist mass is equal to M_{200} (Springel et al., 2005), the density in the outer region near R_{200} falls off more steeply than the technique, by Robertson et al. (2017), used here.

The second requirement was for the inner parts of the profiles to match. For small values of r , the density should be $\rho \sim r^{-1}$. This condition applied to the Hernquist profile, when $r \ll a$, gave the density as $\rho \approx M/(2\pi a^2 r)$. The NFW profile for $r \ll R_s$, where R_s is the scale radius, gave $\rho \approx \delta_c \rho_{crit} R_{200}/(cr)$. The following relation between a and c was obtained,

$$\frac{(R_{200} + a)^2}{a^2} = \frac{3}{400} \frac{\delta_c}{c}, \quad (5.8)$$

where δ_c is a function of c from equation 4.1.

In constructing the distribution of particles to match the density profiles, we required that all particle types, gas and dark matter, have the same mass. This suppresses artificial scattering due to particles of unequal mass where a lighter particle may be ejected from the system due to momentum transfer.

With all particles the same mass and an assumed gas fraction of 17%, we required, for each halo, a minimum of 10^6 particles inside of R_{200} . This ensured there were at least 10^5 gas particles per halo to maintain enough resolution in the simulation in the inner regions of the halos.

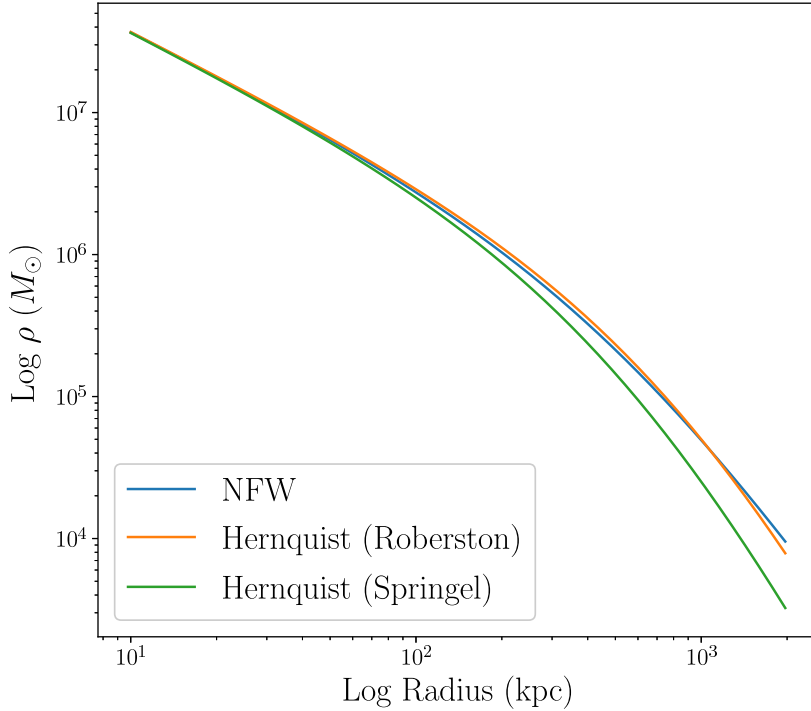


Figure 5.1. Differences in density, ρ , due to different parameter matching schemes are plotted. A target NFW profile of mass $M_{200} = 1.1 \times 10^{15} M_{\odot}$ and concentration $c = 3.5$ is the blue curve. The orange curve more closely matches the NFW profile up to the NFW R_{200} radius, which is the matching prescribed by Robertson et al. (2017) and also used here. The matching scheme used by Springel et al. (2005) (green curve) is not as close of a match to the NFW up to the R_{200} radius. The plot is from 10 kpc to R_{200} .

The Hernquist profile has a finite mass, however, this is only finite by integrating the density to infinity. The construction of a finite particle representation of a smooth function that extends to infinity is not possible unless we restrict the size of the halo to some large radial distance, R_{max} . From equation 5.7, we can specify some maximum fraction of the total mass to obtain a finite maximum radial distance. For $M(r = R_{max})/M = 99\%$, the order of size of R_{max} is $100R_{200}$. We used a $M(r = R_{max})/M = 95\%$, which gives R_{max} to be around $10R_{200}$, which is sufficiently large enough for the simulations here. The excluded mass far outside R_{200} has no significant effect on the dynamics of the collisions.

For the velocity of the dark matter particles we follow the technique used by Robertson et al. (2017). By requiring all particles of a halo to be gravitationally bound, the maximum

velocity a particle is allowed to have is the escape velocity, v_{esc} . For each particle in the halo, a random velocity \mathbf{v} is assigned such that $|\mathbf{v}| \leq v_{esc}$. Note, this is an isotropic velocity distribution which means $\sigma_r = \sigma_\theta = \sigma_\phi$. From the phase space distribution function of a Hernquist density profile the random velocity \mathbf{v} is either rejected or accepted depending on whether a random sample from the distribution function at maximum allowed energy is less than the distribution evaluated at the random velocity energy. Mathematically, the distribution function, as given by Hernquist (1990), is

$$f(E) = \frac{M}{8\sqrt{2}\pi^3 a^3 v_g^3} \frac{1}{(1 - q^2)^{5/2}} (3 \arcsin(q) + q(1 - q^2)^{1/2}(1 - 2q^2)(8q^4 - 8q^2 - 3)), \quad (5.9)$$

where

$$q = \sqrt{\frac{-aE}{GM}}, \quad (5.10)$$

and

$$v_g = \sqrt{\frac{GM}{a}}. \quad (5.11)$$

Then for a random sample, η , from the distribution function at the particle location where f is a maximum, we check to see if that is within the bounds of the distribution function for the randomly sampled velocity \mathbf{v} . We randomly generate η such that $\eta \in [0, f(-GM/(r + a))]$ and then accept the random velocity if $\eta \leq f(-GM/(r + a) + v^2/2)$, otherwise generate a new random velocity to repeat the procedure.

For the gas component, all particle velocities are zero with respect to the core due to the assumption of hydrostatic equilibrium. Each gas particle has an energy per unit mass that can be determined from the one dimensional velocity distribution. From Hernquist (1990) we have the dispersion as

$$\sigma_r = \frac{GM}{12a} \left[\frac{12r(r + a)^3}{a^4} \ln \left(\frac{r + a}{r} \right) - \frac{r}{r + a} \left(25 + 52\frac{r}{a} + 42\frac{r^2}{a^2} + 12\frac{r^3}{a^3} \right) \right]. \quad (5.12)$$

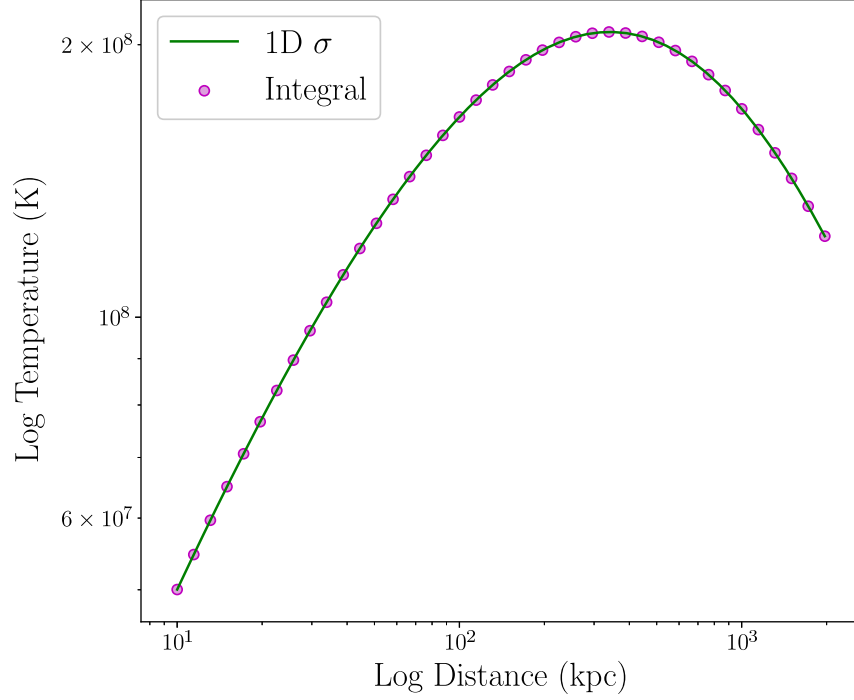


Figure 5.2. A comparison between two formulas for calculating the energy per unit mass. Equation 5.13 is the “1D σ ” line plot, and equation 5.14 is the “integral” circle plot.

Continuing the method used by Robertson et al. (2017), the energy per unit mass is

$$u(r) = \frac{3}{2}\sigma_r^2. \quad (5.13)$$

The energy per unit mass can also be calculated by the following integral obtained from Lage and Farrar (2014),

$$u(r) = \frac{3}{2\rho_g(r)} \int_r^{R_{max}} \frac{\partial\Phi(\xi)}{\partial\xi} \rho_g(\xi) d\xi \quad (5.14)$$

where R_{max} is taken to be some very large number for purposes of numerical integration, ρ_g is the gas density, and Φ is the total potential. A plot of both methods is shown in Figure 5.2 for a halo of mass $M_{200} = 1.1 \times 10^{15} M_\odot$ and concentration $c = 3.5$.

Table 5.1. Particle counts for two halos, A and B, where A is more massive than B, and varying concentrations of A. The halo with the smaller M_{200} determines the particle mass such that there are a total of 10^6 particles inside the volume determined by the corresponding R_{200} . The particle count of the other halo adjusts to this requirement.

	c	N Gas	N DM 2	Total
Halo A $M_{200} = 1.1 \times 10^{15} M_{\odot}$				
Halo B $M_{200} = 0.3 \times 10^{15} M_{\odot}$				
A	2.0	2,066,789	10,090,792	12,157,581
B	3.5	375,693	1,834,268	2,209,961
<hr/>				
A	3.5	1,377,542	6,725,645	8,103,187
B	3.5	375,693	1,834,268	2,209,961
<hr/>				
A	5.0	1,132,526	5,529,393	6,661,919
B	3.5	375,693	1,834,268	2,209,961

5.4 Data

We utilized information obtained from weak lensing (King et al., 2016) to constrain the masses and concentrations. Our parameter space explored various combinations of concentrations.

5.4.1 Particle Counts

The simulations were required to have a minimum particle count of 10^6 for the halo with the smaller M_{200} mass. In Table 5.1, a comparison is made of how the concentration parameter affects particle count.

5.4.2 Simulation Runtime

Two halos were separated by 5 Mpc at the start of the simulation. Each halo was given a bulk velocity by assuming that each M_{200} acted like a point mass falling from rest at infinity.

The halos were allowed to have an on-axis collision to simplify the model for purposes of looking at the bulk motions of the halos. Abell 2146 does not appear to be a perfect on-axis collision as evidenced by a plume of gas in X-ray observations (Russell et al., 2012),

however, the asymmetry is small enough that the separation distance between clusters to eject a perpendicular plume of gas on one side is on the order of the core size (Russell et al., 2012). Early tests of different density profiles showed perpendicular plumes for on-axis collisions.

The simulation runtime was approximately 4 gigayears. The internal GADGET-2 code units for time has 1.0 unit of code time equal to 9.8×10^8 yr. This allowed the halos to have at least one core passage.

5.5 Procedure and Analysis

The data from the simulations was analyzed in multiple steps. First, the mass peaks were identified post collision. By leveraging the findings from the strong lensing (Coleman et al., 2017) and weak lensing (King et al., 2016), we have constraints on the separation. For a given snapshot of the simulation, peaks in the dark matter were determined and are further discussed in section 5.5.1. Figure 5.3 plots peak separation for each snapshot of the simulation written to disk.

For instances after first core passage where the separation distance between peaks was larger than observed, we rotate the system by some angle θ with respect to the plane of the sky so that the projected separation distance matches observation. Figure 5.4 illustrates how two objects can have a larger separation than observed due to projection effects.

X-ray maps were computed using the rotation angle obtained from the peak detection. Peaks in the X-ray were compared with the peak location from observational data provided by the *Chandra X-ray Observatory*. The locations of the shock fronts seen in observation data were used to demarcate bounds from which a goodness of fit were determined. Section 5.5.2 details the creation of synthetic maps and how the X-ray data was used.

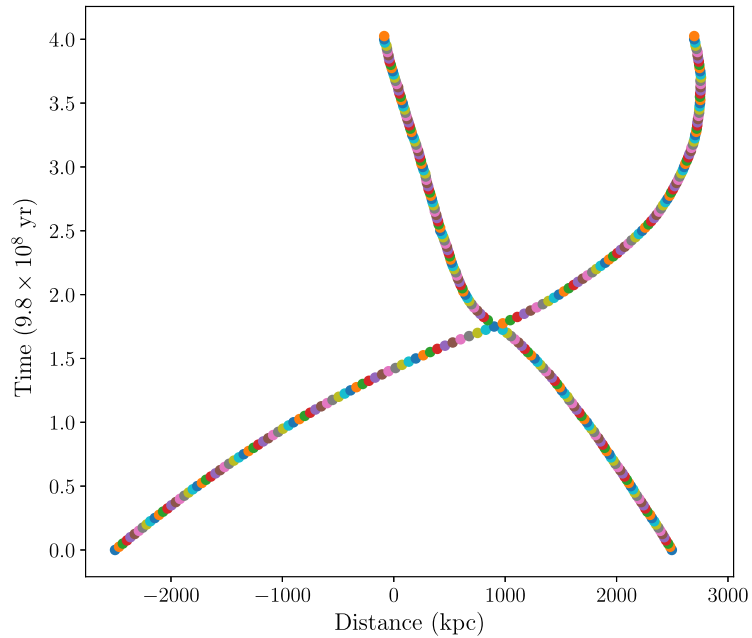


Figure 5.3. The separation distance between peaks in the dark matter. Time is on the vertical axis, distance on the horizontal axis. Core passage occurs at roughly $t = 1.7$ in internal time units. The more massive halo A starts on the right at time $t = 0$ at location $X = 2500$ kpc. Halo B starts at $x = -2500$ kpc and is on the left. At the end of the simulation halo A is on the left and halo B is on the right.

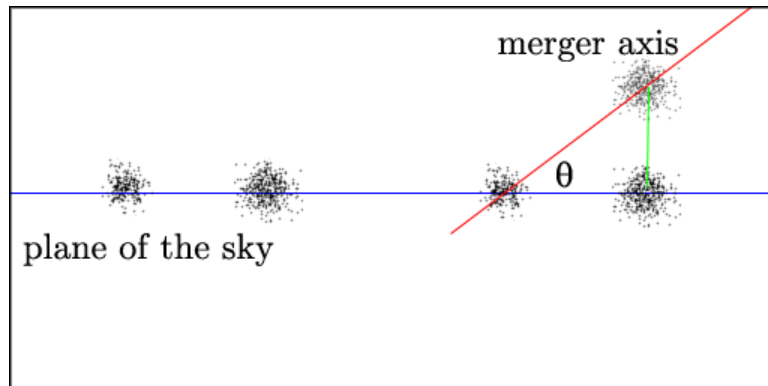


Figure 5.4. Left hand side, in the plane of the sky we see objects separated by some distance. Right hand side, two objects can have a separation larger than observed if tilted some angle θ with respect to the surface their positions are projected on, in this case, the plane of the sky.

5.5.1 Finding Peaks

There are various robust techniques for finding halos in cosmological simulations (Knollmann and Knebe, 2009; Gill et al., 2004; Davis et al., 1985; Behroozi et al., 2013; Riebe et al., 2013; Klypin and Holtzman, 1997) . Such robustness isn't needed for simply finding the peaks in the dark matter. Generally speaking, halo finding algorithms attempt to identify clusters by determining which particles are part of the cluster. The identification of all particles bound to a halo is not needed for simply identifying the core of a cluster, especially given the starting conditions employed here of only two clusters. We employed a much simpler technique for identifying halo centers.

The dark matter components of the simulations were found to be more resilient, in terms of disruption, compared with the gas component. For our peak detection, we looked at only the dark matter particles. Along the axis of collision, a long volume of particles was extracted. The end cap area of the volume was 10 kpc by 10 kpc, with a length extending 10,000 kpc. The dark matter particles were then binned into $10 \text{ kpc}^2 \times 40 \text{ kpc}$ subvolumes. Peak detection was done in two steps, first a coarse resolution and then a fine resolution.

For the coarse peak detection an average of the number of particles per bin was calculated, excluding the bin with the maximum. The reason we excluded the bin with the maximum number of particles is due to alignment effects with binning densities that have a sharp cusp at the peak location. Specifically, for a volume element centered on a peak with N particles in the bin, an alignment dividing this peak at half a volume length away would give two adjacent bins each roughly $N/2$ particles. For cusps, N can be significantly larger than immediately adjacent bins. Next, each bin was considered a possible peak if the number of particles inside the bin was 5 times the average. This multiplier is a parameter that can be modified to adjust the sensitivity of peak detection. A finite difference was calculated between adjacent bins, effectively giving the derivative of the histogram. Sign changes were then identified in the derivative such that the bin is an inflection point where the derivative changes sign

from positive to negative. A secondary derivative check is performed with the average derivative for two bins before and after the possible peak. This filters noise that may occur during or after collision of cores. Stated mathematically, for some number counts in bins $\{\dots, n_{i-2}, n_{i-1}, n_i, n_{i+1}, n_{i+2}, \dots\}$, we require that $n_i > 5\bar{n}$ and $(n_i - n_{i-1}) > 0; (n_{i+1} - n_i) < 0$ and $(n_i - n_{i-2}) > 0; (n_{i+2} - n_i) < 0$, where n_i is the number count in bin i and \bar{n} is the average without the maximum as described earlier.

The second pass was to take each identified candidate from the coarse sample and consider the maximum number density around the point of interest. A sphere of radius 10 kpc was swept through the volume of interest and two immediate neighboring volumes at an increment of 1 kpc. The maximum number count in this swept volume indicated the location of the peak ± 1 kpc.

5.5.2 Generating X-ray maps

Synthetic X-ray maps were generated from simulation data using the software PHOX following the prescription of Biffi et al. (2012, 2013) utilizing the python implementation, known as PYXSIM, from John A. ZuHone et al. (2014).

PHOX uses the gas component from simulations as input and creates a large sample of photons in 3D space, which is a discretization of emissivity. For our thermal emission model, we used APEC (Smith et al., 2001) which is a “collisional-radiative plasma code” that models the spectra of hot plasma (Smith et al., 2001), such as that associated with galaxy clusters. We looked at photon energies that corresponded with the camera used on *Chandra X-ray Observatory* for observation 12245, specifically 0.1 keV to 7 keV. From large photon databases, a subsample of photons were selected using a Monte Carlo approach. The observation location was chosen such that, in projection, the separation between dark matter peaks are separated by 450 kpc. The synthetic photon maps were convolved with the ACIS I instrument response and was integrated for 450 ks. For a 1.5 arcmin radius region

of *Chandra X-ray Observatory* observation 12245, an effective collection area used for the synthetic simulation was 500 cm^2 . This collection area, which corresponds with an energy of 1.5 keV, is where we expect the majority of photons given the instrument response of *Chandra X-ray Observatory* during observation 12245.

Since X-ray observations are photon limited we were limited by low number statistics. However, since the simulation data can be thought of as an ideal case, we created multiple mock X-ray maps for each point of observation and averaged them. This was simply the application of the law of large numbers from statistics such that we could smooth out the random noise in the synthetic maps. The averages of different numbers of X-ray maps were tested. An average of 10 maps was sufficient to suppress noise in low photon count regions.

For the purposes of matching the peak and shock fronts in the X-ray data to simulation, we considered a bisecting slice that intersected the peak in the X-ray and BCG-B. This slice gives the locations of the X-ray peak and the locations of the shock fronts. Figure 5.5 illustrates the slice through the peak of the X-ray. We also constructed slices in the simulated X-ray maps that intersected the peaks in the dark matter. We aligned the identified location of the dark matter peak from the strong lensing analysis (Coleman et al., 2017), which is coincident with BCG-A, with the a dark matter peak identified from simulations. The alignment in the dark matter signal constrained the alignment in X-ray. Similar to Lage and Farrar (2014), we considered the following expression for the goodness of fit for the X-ray signal,

$$\chi_{dof}^2 = \frac{1}{N} \sum_{i=1}^N \frac{(n_{sim,i} - n_{obs,i})^2}{\sigma_{sim}^2 + \sigma_{obs}^2}, \quad (5.15)$$

where this is a χ^2 per degree of freedom, N is the number of pixels in the slice, n_{sim} is the photon count in the simulation X-ray map, n_{obs} is the photon count from the observed *Chandra X-ray Observatory* data, and $\sigma_{sim}^2 + \sigma_{obs}^2$ is the total error with an error on a pixel $\sigma_i = \sqrt{n_i}$. The error $\sigma_i = \sqrt{n_i}$ is due to the use of Poisson statistics because of the low number count in each pixel or bin. The pixels examined begin at one shock front and end

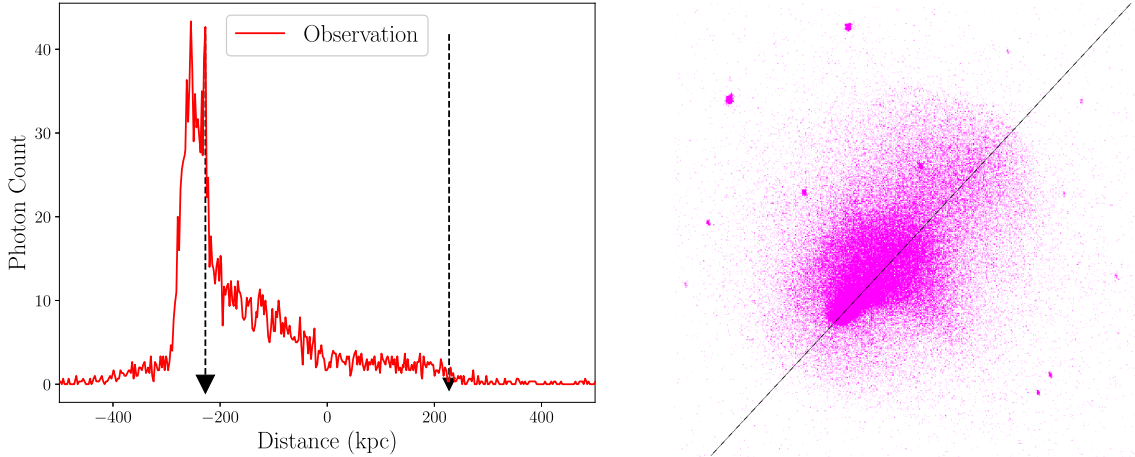


Figure 5.5. Left, a slice of pixel counts from the X-ray data obtained from *Chandra X-ray Observatory*. The vertical line on the left is the location of BCG-A, the vertical line on the right is the location of BCG-B. The upstream shock front is coincident with BCG-B. The bow shock is to the left of the X-ray peak. The sharp spike at the location of BCG-A is due to an active galactic nuclei. Right, the X-ray image of Abell 2146. The bright peak is in the lower left of the image.

at the other shock front. Pixels where the combined photon count from simulation and observation is zero were excluded from the calculation.

5.6 Results and Analysis

The behavior of the dark matter peaks in terms of concentration is of interest. In Figure 5.6, we show a fixed concentration for halo A, the more massive halo with $M_{200} = 1.1 \times 10^{15} M_{\odot}$, compared to varying concentrations of the less massive halo B with $M_{200} = 0.3 \times 10^{15} M_{\odot}$. In the case where the concentration of halo A is fixed at $c_A = 2.0$, we see that at the end of the simulation, at time¹ $t = 4.0$, the position of halo B, with concentration $c_B = 2.0$, is closer to halo A than with $c_B = 5.0$. This is opposite to the case when halo A has a higher concentration $c_A = 5.0$; the more concentrated halo B, with $c_B = 5.0$, is closer to halo A

¹The time given is in internal GADGET-2 time units.

than when $c_B = 2.0$ at the end of the simulation. In all instances, the behavior of the heavier halo A experienced a deflection during core passage while the behavior of halo B is more varied, as shown in Figure 5.7.

However, when one considers the behavior of a varying concentration of halo A on a constant concentration of halo B, a more consistent pattern emerges. In Figure 5.8, we show plots where in each panel the concentration of halo B is kept constant and the concentration of the more massive halo A is varied. In all instances, the behavior of halo B has, at the end of the simulation, a closer separation when the halo A is more concentrated. Halo B is encountering more matter when halo A is more concentrated, and this simply slows down halo B with respect to halo A.

If the simulation were to evolve past the cutoff time of our simulation, we would expect to see more deviation in the behavior of halo A.

The behavior of the dark matter peaks, with regard to concentration, is a prelude to the behavior of the X-ray peak. Our results indicate that the location of the X-ray peak is highly dependent on the concentrations of the halos in the merger. From equation 4.2, the set of parameters that gave a value of χ^2 closest to unity was, for halo A and halo B respectively, concentrations $c_A = 3.5$ and $c_B = 2.0$, at a time of roughly 1 Gyr after first core passage with a merger axis angle with respect to the plane of the sky of 77.1° . In Figure 5.9, the X-ray simulation has a peak in X-ray slightly ahead of BCG-A with a characteristic wake in the direction of the other halo similar to feature observed in the *Chandra X-ray Observatory* observation.

The X-ray signal in the best fit model does not have well-defined shock fronts due to this time being much later than first core passage and also having a rather large angle with respect to the plane of the sky. The projection angle grows larger rather quickly with our simulation outputs. After first core passage, the distance a typical core moves between adjacent snapshots is roughly 100 kpc. To constrain the separation between the peaks in

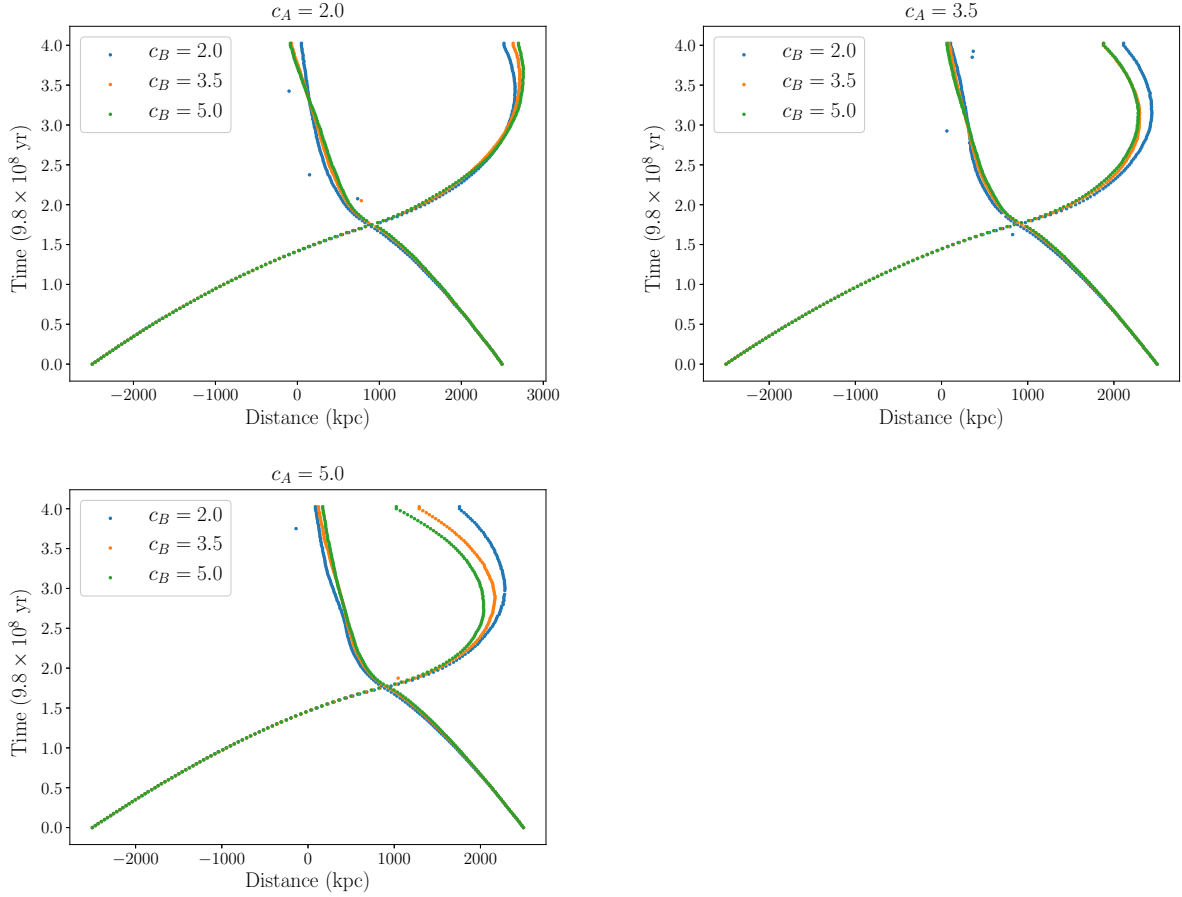


Figure 5.6. The more massive halo A starts at 2500 kpc, the less massive halo B starts at -2500 kpc. The halo A concentration is constant in each of the plots while the halo B concentration is 2.0, 3.5, and 5.0.

the dark matter to 450 kpc means that for some time step, t_i , when the separation distance is $\Delta x_i = 450$ kpc, the next time step at t_{i+1} will have $\Delta x_{i+1} = 550$ kpc. To view that separation in projection is already a 35° angle with respect to the plane of the sky. Any shock fronts present quickly disappear due to projection effects.

If we consider the local minima of equation 4.2 instead, we can identify cases where the peak in the X-ray is distinctly ahead of the peak of halo A. For a higher concentration of halo A, $c_A = 5.0$ and $c_B = 2.0$, we have at an earlier time at about 0.68 Gyr after core

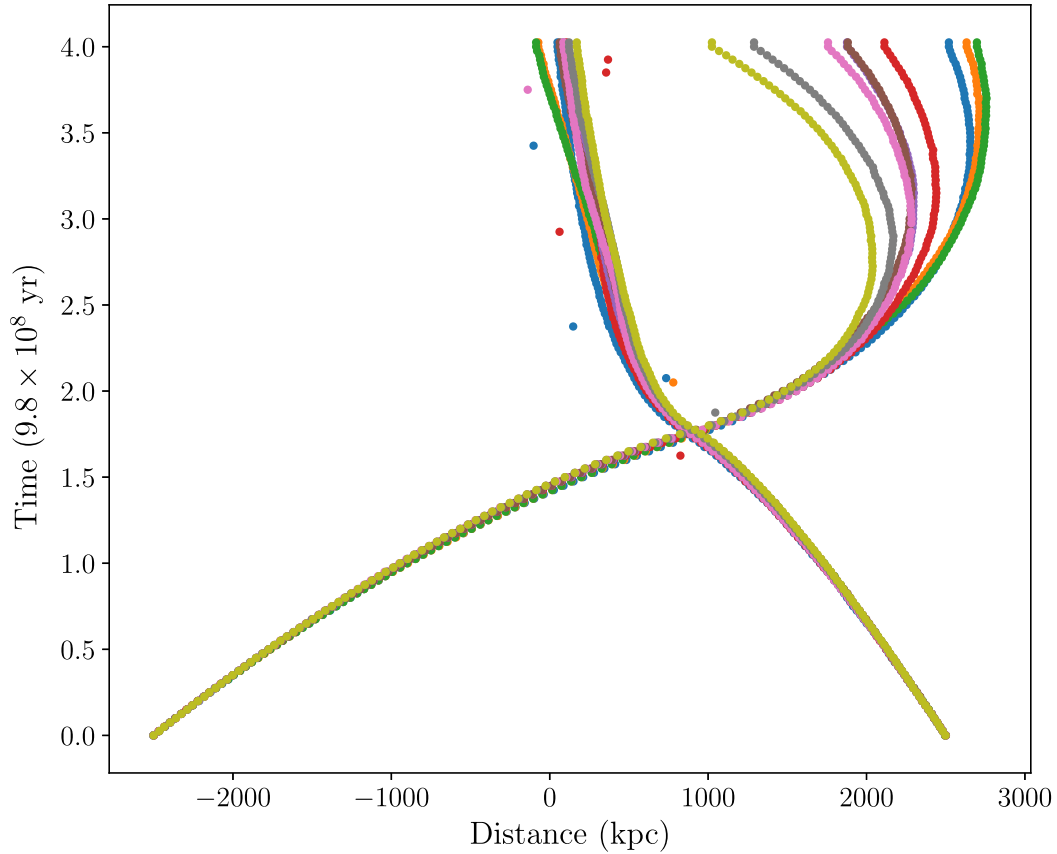


Figure 5.7. Plotted are the separation distances versus simulation time for all combinations of concentrations where the mass ratio is 11:3.5. The more massive halo A starts at 2500 kpc, the less massive halo B starts at -2500 kpc. The behavior of halo B varies more after collision than does halo A.

passage, the result shown in Figure 5.10. Again, the angle of inclination with respect to the plane of the sky is rather large.

Regarding the dependence of the X-ray peak on concentration and mass, we found that after first core passage the initial peak in the X-ray would be closer to the peak in dark matter for halo B when halo B was more concentrated than halo A. We also noticed that for a high concentration halo A, the peak in the X-ray would follow halo A when halo B had a low concentration, and it would follow halo B when halo B had a high concentration.

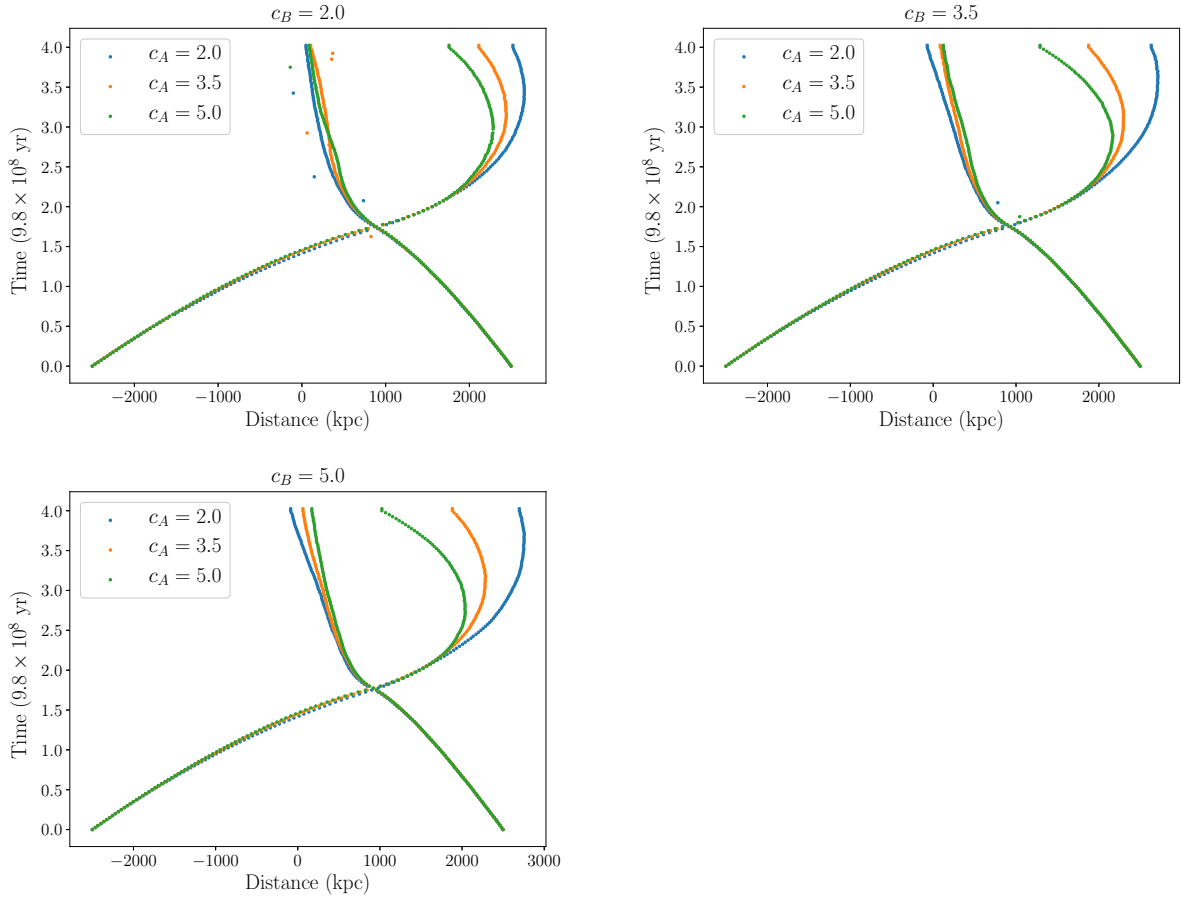


Figure 5.8. The more massive halo A starts at 2500 kpc, the less massive halo B starts at -2500 kpc. The halo B concentration is constant in each of the plots while the halo A concentration is 2.0, 3.5, and 5.0.

5.7 Conclusion

Different concentrations of Hernquist profiles were used to create initial conditions for two halos as a model for two galaxy clusters, each consisting of a dark matter component and a gaseous component that represents the intracluster medium. The clusters were allowed to collide using GADGET-2 as the N-body SPH solver. Peaks in the dark matter component were identified and used for alignment of mock X-ray data. The mock X-ray data was created with PYXSIM, a PYTHON wrapper for PHOX.

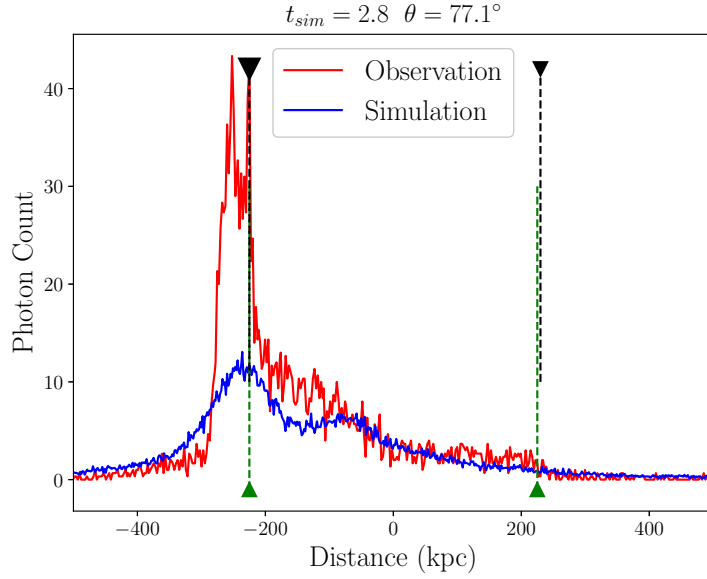


Figure 5.9. The best fit according to our χ^2 calculation gives parameters $c_A = 3.5$, $c_B = 2.0$. The black triangles indicate the locations of the peaks in the dark matter from observation. The green triangles mark the locations of the dark matter peaks in the simulation.

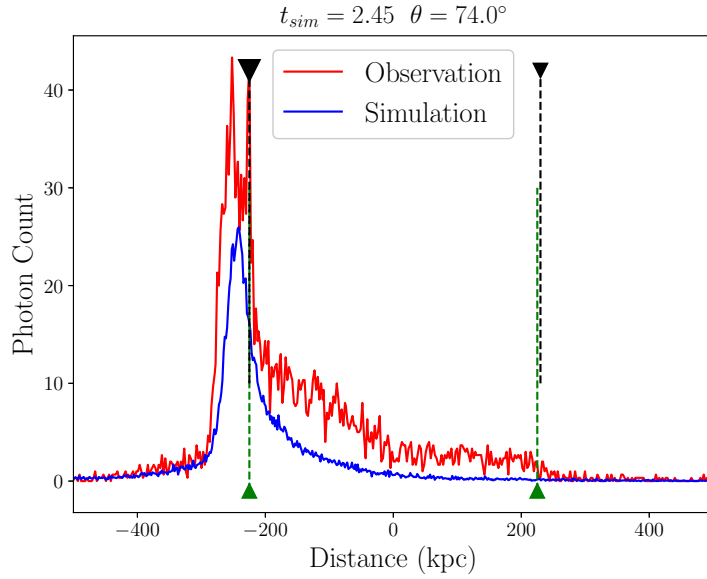


Figure 5.10. For concentrations $c_A = 5.0$ and $c_B = 2.0$ the peak in X-ray is ahead of the peak in dark matter. The black triangles indicate the locations of the peaks in the dark matter from observation. The green triangles mark the locations of the dark matter peaks in the simulation.

Results from simulation indicate that it is possible to have peaks in X-ray ahead of the dark matter component of the more massive halo, however, this occurred at a much later time and with a large angle of inclination with respect to the plane of the sky, which seems at odds with the observation of shock fronts. White et al. (2015), Russell et al. (2012), and Hlavacek-Larrondo et al. (2018) have consistent age measurements for this halo of no more than 0.3 Gyr after core passage. However, simulations using the Monte Carlo technique of Dawson (2014) indicated that the merger may be older.

CHAPTER 6

SUMMARY AND CONCLUDING REMARKS

We live in a universe that can be described with rather simple ideas, such as the notion that there was an energetic expansion where the matter of the universe eventually cooled, and through tiny fluctuations in density, created the structures that we see today. The notion of gravity pulling things together leads to the hierarchical formation of structure in the universe. Simple ideas lead to complex processes.

Our desire for understanding the universe has led us to try to make sense of what we see, and also of what we don't see. There is a quote attributed to Albert Einstein about simplicity. "Everything should be made as simple as possible, but not simpler." The work presented here has attempted this.

Abell 2146 is a fascinating merger of galaxy clusters. It was the first merger system to be discovered with two shock fronts visible (Russell et al., 2010, 2012). The confirmation that the peak in the X-ray signal is leading dark matter was an astonishing result. This was achieved with the simple idea that the gravity from both luminous and dark matter can bend light. By looking at how gravity bends the light, we can identify the matter even when it can not be seen. Simulations were constructed with simple models of gas and dark matter that revealed that Abell 2146 will not give up its secrets so easily.

In Chapter 4, we performed a strong lensing analysis of Abell 2146. Different models were explored which allowed for investigating signals seen in the weak lensing analysis. Results were verified with two different techniques for studying the mass distribution of Abell 2146. We found the centroid for the dark matter component closest to the peak in the X-ray was trailing behind the gas component.

In Chapter 5, we studied the bulk motion of the gas and dark matter components using hydrodynamic simulations. We found that the concentration of the matter affects the bulk flow of the gas and the location of the X-ray signal. The timescale required in simulations

to achieve the observed separation of the dark matter along with a bright peak in the X-ray that is leading the more massive dark matter component is found to be larger than theorized by other studies.

More work needs to be done on simulating this system to investigate the physics of the intracluster medium. The dynamics of the plasma are affected by magnetic fields. Expanding the simulations complexity from hydrodynamic to magnetohydrodynamic will give a richer understanding of the system. Individual features observed in the X-ray, such as the plume of gas that seems to have been stripped from an off axis merger, the existence of a ram pressure striped tail, and the length and thickness of the shock fronts need to be investigated. These are all probes to learn more about diffusion, viscosity, thermal conduction, and electron-ion equilibration within the intracluster medium.

REFERENCES

- Allen, S. W., A. E. Evrard, and A. B. Mantz (2011, September). Cosmological Parameters from Observations of Galaxy Clusters. *Annual Review of Astronomy and Astrophysics* *49*, 409–470.
- AMI Consortium, C. Rodríguez-Gonzálvez, M. Olamaie, M. L. Davies, A. C. Fabian, F. Feroz, T. M. O. Franzen, K. J. B. Grainge, M. P. Hobson, N. Hurley-Walker, A. N. Lasenby, G. G. Pooley, H. R. Russell, J. S. Sanders, R. D. E. Saunders, A. M. M. Scaife, M. P. Schammel, P. F. Scott, T. W. Shimwell, D. J. Titterington, E. M. Waldram, and J. T. L. Zwart (2011, July). Sunyaev-Zel’dovich observation of the Bullet-like cluster Abell 2146 with the Arcminute Microkelvin Imager. *MNRAS* *414*, 3751–3763.
- Behroozi, P. S., R. H. Wechsler, and H.-Y. Wu (2013, January). The ROCKSTAR Phase-space Temporal Halo Finder and the Velocity Offsets of Cluster Cores. *ApJ* *762*, 109.
- Bertin, E. and S. Arnouts (1996, June). SExtractor: Software for source extraction. *A&AS* *117*, 393–404.
- Biffi, V., K. Dolag, and H. Böhringer (2013, January). Investigating the velocity structure and X-ray observable properties of simulated galaxy clusters with PHOX. *MNRAS* *428*, 1395–1409.
- Biffi, V., K. Dolag, H. Böhringer, and G. Lemson (2012, March). Observing simulated galaxy clusters with PHOX: a novel X-ray photon simulator. *MNRAS* *420*, 3545–3556.
- Bryan, G. L., M. L. Norman, B. W. O’Shea, T. Abel, J. H. Wise, M. J. Turk, D. R. Reynolds, D. C. Collins, P. Wang, S. W. Skillman, B. Smith, R. P. Harkness, J. Bordner, J.-h. Kim, M. Kuhlen, H. Xu, N. Goldbaum, C. Hummels, A. G. Kritsuk, E. Tasker, S. Skory, C. M. Simpson, O. Hahn, J. S. Oishi, G. C. So, F. Zhao, R. Cen, Y. Li, and The Enzo Collaboration (2014, April). ENZO: An Adaptive Mesh Refinement Code for Astrophysics. *ApJS* *211*, 19.
- Canning, R. E. A., H. R. Russell, N. A. Hatch, A. C. Fabian, A. I. Zabludoff, C. S. Crawford, L. J. King, B. R. McNamara, S. Okamoto, and S. I. Raimundo (2012, March). Riding the wake of a merging galaxy cluster. *MNRAS* *420*, 2956–2968.
- Chandrasekhar, S. (1949, Jul). Brownian motion, dynamical friction, and stellar dynamics. *Rev. Mod. Phys.* *21*, 383–388.
- Clowe, D., M. Bradač, A. H. Gonzalez, M. Markevitch, S. W. Randall, C. Jones, and D. Zaritsky (2006, September). A Direct Empirical Proof of the Existence of Dark Matter. *ApJ* *648*, L109–L113.

- Clowe, D., A. Gonzalez, and M. Markevitch (2004, April). Weak-Lensing Mass Reconstruction of the Interacting Cluster 1E 0657-558: Direct Evidence for the Existence of Dark Matter. *ApJ* 604, 596–603.
- Coleman, J. E., L. J. King, M. Oguri, H. R. Russell, R. E. A. Canning, A. Leonard, R. Santana, J. A. White, S. A. Baum, D. I. Clowe, A. Edge, A. C. Fabian, B. R. McNamara, and C. P. O’Dea (2017, January). The mass distribution of the unusual merging cluster Abell 2146 from strong lensing. *MNRAS* 464, 2469–2480.
- Cossins, P. J. (2010, July). *Smoothed Particle Hydrodynamics*. Ph. D. thesis, PhD Thesis, 2010.
- Crawford, C. S., S. W. Allen, H. Ebeling, A. C. Edge, and A. C. Fabian (1999, July). The ROSAT Brightest Cluster Sample - III. Optical spectra of the central cluster galaxies. *MNRAS* 306, 857–896.
- Davis, M., G. Efstathiou, C. S. Frenk, and S. D. M. White (1985, May). The evolution of large-scale structure in a universe dominated by cold dark matter. *ApJ* 292, 371–394.
- Dawson, W. A. (2014, July). MCMAC: Monte Carlo Merger Analysis Code. Astrophysics Source Code Library.
- Dodelson, S. (2003). *Modern Cosmology*. Academic Press.
- Dodelson, S., E. I. Gates, and M. S. Turner (1996, October). Cold Dark Matter. *Science* 274, 69–75.
- Elíasdóttir, Á., M. Limousin, J. Richard, J. Hjorth, J.-P. Kneib, P. Natarajan, K. Pedersen, E. Jullo, and D. Paraficz (2007, October). Where is the matter in the Merging Cluster Abell 2218? Unpublished.
- Gill, S. P. D., A. Knebe, and B. K. Gibson (2004, June). The evolution of substructure - I. A new identification method. *MNRAS* 351, 399–409.
- Hallman, E. J. and M. Markevitch (2004, August). Chandra Observation of the Merging Cluster A168: A Late Stage in the Evolution of a Cold Front. *ApJL* 610, L81–L84.
- Hamer, S. L., A. C. Edge, A. M. Swinbank, R. J. Wilman, H. R. Russell, A. C. Fabian, J. S. Sanders, and P. Salomé (2012, April). The relation between line emission and brightest cluster galaxies in three exceptional clusters: evidence for gas cooling from the intracluster medium. *MNRAS* 421, 3409–3417.
- Harvey, D., R. Massey, T. Kitching, A. Taylor, and E. Tittley (2015, March). The nongravitational interactions of dark matter in colliding galaxy clusters. *Science* 347, 1462–1465.

- Hernquist, L. (1990, June). An analytical model for spherical galaxies and bulges. *ApJ* 356, 359–364.
- Hirt, C. W., A. A. Amsden, and J. L. Cook (1974, March). An Arbitrary Lagrangian-Eulerian Computing Method for All Flow Speeds. *Journal of Computational Physics* 14, 227–253.
- Hlavacek-Larrondo, J., M.-L. Gendron-Marsolais, D. Fecteau-Beaucage, R. J. van Weeren, H. R. Russell, A. Edge, M. Olamaie, C. Rumsey, L. King, A. C. Fabian, B. McNamara, M. Hogan, M. Mezcuca, and G. Taylor (2018, April). Mystery solved: discovery of extended radio emission in the merging galaxy cluster Abell 2146. *MNRAS* 475, 2743–2753.
- Hogg, D. W. (1999, May). Distance measures in cosmology. *ArXiv Astrophysics e-prints*.
- Hudson, D. S., R. Mittal, T. H. Reiprich, P. E. J. Nulsen, H. Andernach, and C. L. Sarazin (2010, April). What is a cool-core cluster? a detailed analysis of the cores of the X-ray flux-limited HIFLUGCS cluster sample. *A&P* 513, A37.
- Jaffe, W. (1983, March). A simple model for the distribution of light in spherical galaxies. *MNRAS* 202, 995–999.
- John A. ZuHone, Veronica Biffi, Eric J. Hallman, Scott W. Randall, Adam R. Foster, and Christian Schmid (2014). Simulating X-ray Observations with Python. In Stéfan van der Walt and James Bergstra (Eds.), *Proceedings of the 13th Python in Science Conference*, pp. 103 – 110.
- Jullo, E., J.-P. Kneib, M. Limousin, Á. Elíasdóttir, P. J. Marshall, and T. Verdugo (2007, December). A Bayesian approach to strong lensing modelling of galaxy clusters. *New Journal of Physics* 9, 447.
- Keeton, C. R. (2001, February). A Catalog of Mass Models for Gravitational Lensing. *ArXiv Astrophysics e-prints*.
- King, L. J., D. I. Clowe, J. E. Coleman, H. R. Russell, R. Santana, J. A. White, R. E. A. Canning, N. J. Deering, A. C. Fabian, B. E. Lee, B. Li, and B. R. McNamara (2016, March). The Distribution of Dark and Luminous Matter in the Unique Galaxy Cluster Merger Abell 2146. *MNRAS*.
- Klypin, A. and J. Holtzman (1997, December). Particle-Mesh code for cosmological simulations. *ArXiv Astrophysics e-prints*.
- Kneib, J.-P., R. S. Ellis, I. Smail, W. J. Couch, and R. M. Sharples (1996, November). Hubble Space Telescope Observations of the Lensing Cluster Abell 2218. *ApJ* 471, 643.
- Knollmann, S. R. and A. Knebe (2009, June). AHF: Amiga’s Halo Finder. *ApJS* 182, 608–624.

- Kunz, M. W., A. A. Schekochihin, S. C. Cowley, J. J. Binney, and J. S. Sanders (2011, February). A thermally stable heating mechanism for the intracluster medium: turbulence, magnetic fields and plasma instabilities. *MNRAS* *410*, 2446–2457.
- Lage, C. and G. Farrar (2014, June). Constrained Simulation of the Bullet Cluster. *ApJ* *787*, 144.
- Lemson, G. and t. Virgo Consortium (2006, August). Halo and Galaxy Formation Histories from the Millennium Simulation: Public release of a VO-oriented and SQL-queryable database for studying the evolution of galaxies in the LambdaCDM cosmogony. *ArXiv Astrophysics e-prints*.
- Limousin, M., J. Richard, E. Jullo, J.-P. Kneib, B. Fort, G. Soucail, Á. Elíasdóttir, P. Natarajan, R. S. Ellis, I. Smail, O. Czoske, G. P. Smith, P. Hudelot, S. Bardeau, H. Ebeling, E. Egami, and K. K. Knudsen (2007, October). Combining Strong and Weak Gravitational Lensing in Abell 1689. *ApJ* *668*, 643–666.
- Macario, G., M. Markevitch, S. Giacintucci, G. Brunetti, T. Venturi, and S. S. Murray (2011, February). A Shock Front in the Merging Galaxy Cluster A754: X-ray and Radio Observations. *ApJ* *728*, 82.
- Markevitch, M., A. H. Gonzalez, D. Clowe, A. Vikhlinin, W. Forman, C. Jones, S. Murray, and W. Tucker (2004, May). Direct Constraints on the Dark Matter Self-Interaction Cross Section from the Merging Galaxy Cluster 1E 0657-56. *ApJ* *606*, 819–824.
- Markevitch, M., A. H. Gonzalez, L. David, A. Vikhlinin, S. Murray, W. Forman, C. Jones, and W. Tucker (2002, March). A Textbook Example of a Bow Shock in the Merging Galaxy Cluster 1E 0657-56. *ApJ* *567*, L27–L31.
- Markevitch, M. and A. Vikhlinin (2007, May). Shocks and cold fronts in galaxy clusters. *Phys Rep* *443*, 1–53.
- Massey, R., L. Williams, R. Smit, M. Swinbank, T. D. Kitching, D. Harvey, M. Jauzac, H. Israel, D. Clowe, A. Edge, M. Hilton, E. Jullo, A. Leonard, J. Liesenborgs, J. Merten, I. Mohammed, D. Nagai, J. Richard, A. Robertson, P. Saha, R. Santana, J. Stott, and E. Tittley (2015, June). The behaviour of dark matter associated with four bright cluster galaxies in the 10 kpc core of Abell 3827. *MNRAS* *449*, 3393–3406.
- Navarro, J. F., C. S. Frenk, and S. D. M. White (1996, May). The Structure of Cold Dark Matter Halos. *ApJ* *462*, 563.
- Oguri, M. (2010, August). The Mass Distribution of SDSS J1004+4112 Revisited. *PASJ* *62*, 1017–1024.

- Ostriker, J. P. and P. J. Steinhardt (1995, May). Cosmic Concordance. *ArXiv Astrophysics e-prints*.
- Pathria, R. K. and P. D. Beale (2011). *Statistical Mechanics* (Thrid ed.). Academic Press.
- Postman, M., D. Coe, N. Benítez, L. Bradley, T. Broadhurst, M. Donahue, H. Ford, O. Graur, G. Graves, S. Jouvel, A. Koekemoer, D. Lemze, E. Medezinski, A. Molino, L. Moustakas, S. Ogaz, A. Riess, S. Rodney, P. Rosati, K. Umetsu, W. Zheng, A. Zitrin, M. Bartelmann, R. Bouwens, N. Czakon, S. Golwala, O. Host, L. Infante, S. Jha, Y. Jimenez-Teja, D. Kelson, O. Lahav, R. Lazkoz, D. Maoz, C. McCully, P. Melchior, M. Meneghetti, J. Merten, J. Moustakas, M. Nonino, B. Patel, E. Regös, J. Sayers, S. Seitz, and A. Van der Wel (2012, April). The Cluster Lensing and Supernova Survey with Hubble: An Overview. *ApJS* 199, 25.
- Press, W. H., W. T. Teukolsky, S. A. Vetterling, and B. P. Flannery (1992). *Numerical Recipes in C*. Cambridge University Press.
- Price, D. (2005, July). *Smoothed Particle Hydrodynamics*. Ph. D. thesis, PhD Thesis, 2005.
- Randall, S. W., M. Markevitch, D. Clowe, A. H. Gonzalez, and M. Bradač (2008, June). Constraints on the Self-Interaction Cross Section of Dark Matter from Numerical Simulations of the Merging Galaxy Cluster 1E 0657-56. *ApJ* 679, 1173–1180.
- Riebe, K., A. M. Partl, H. Enke, J. Forero-Romero, S. Gottlöber, A. Klypin, G. Lemson, F. Prada, J. R. Primack, M. Steinmetz, and V. Turchaninov (2013, August). The MultiDark Database: Release of the Bolshoi and MultiDark cosmological simulations. *Astronomische Nachrichten* 334, 691–708.
- Robertson, A., R. Massey, and V. Eke (2017, February). What does the Bullet Cluster tell us about self-interacting dark matter? *MNRAS* 465, 569–587.
- Rosswog, S. (2009, April). Astrophysical smooth particle hydrodynamics. *New Astronomy Reviews* 53, 78–104.
- Russell, H. R., B. R. McNamara, J. S. Sanders, A. C. Fabian, P. E. J. Nulsen, R. E. A. Canning, S. A. Baum, M. Donahue, A. C. Edge, L. J. King, and C. P. O’Dea (2012, June). Shock fronts, electron-ion equilibration and intracluster medium transport processes in the merging cluster Abell 2146. *MNRAS* 423, 236–255.
- Russell, H. R., J. S. Sanders, A. C. Fabian, S. A. Baum, M. Donahue, A. C. Edge, B. R. McNamara, and C. P. O’Dea (2010, August). Chandra observation of two shock fronts in the merging galaxy cluster Abell 2146. *MNRAS* 406, 1721–1733.

- Russell, H. R., R. J. van Weeren, A. C. Edge, B. R. McNamara, J. S. Sanders, A. C. Fabian, S. A. Baum, R. E. A. Canning, M. Donahue, and C. P. O’Dea (2011, October). A merger mystery: no extended radio emission in the merging cluster Abell 2146. *MNRAS* *417*, L1–L5.
- Sanderson, A. J. R., A. C. Edge, and G. P. Smith (2009, October). LoCuSS: the connection between brightest cluster galaxy activity, gas cooling and dynamical disturbance of X-ray cluster cores. *MNRAS* *398*, 1698–1705.
- Schneider, P. (2003, June). Gravitational lensing as a probe of structure. *ArXiv Astrophysics e-prints*.
- Schneider, P., J. Ehlers, and E. E. Falco (1995). *Gravitational Lenses*. Springer-Verlag.
- Sharon, K., M. D. Gladders, J. R. Rigby, E. Wuyts, M. B. Bayliss, T. L. Johnson, M. K. Florian, and H. Dahle (2014, November). The Mass Distribution of the Strong Lensing Cluster SDSS J1531+3414. *ApJ* *795*, 50.
- Smith, R. K., N. S. Brickhouse, D. A. Liedahl, and J. C. Raymond (2001, August). Collisional Plasma Models with APEC/APED: Emission-Line Diagnostics of Hydrogen-like and Helium-like Ions. *ApJL* *556*, L91–L95.
- Smoot, G. F., C. L. Bennett, A. Kogut, E. L. Wright, J. Aymon, N. W. Boggess, E. S. Cheng, G. de Amici, S. Gulkis, M. G. Hauser, G. Hinshaw, P. D. Jackson, M. Janssen, E. Kaita, T. Kelsall, P. Keegstra, C. Lineweaver, K. Loewenstein, P. Lubin, J. Mather, S. S. Meyer, S. H. Moseley, T. Murdock, L. Rokke, R. F. Silverberg, L. Tenorio, R. Weiss, and D. T. Wilkinson (1992, September). Structure in the COBE differential microwave radiometer first-year maps. *ApJL* *396*, L1–L5.
- Springel, V. (2005, December). The cosmological simulation code GADGET-2. *MNRAS* *364*, 1105–1134.
- Springel, V. (2010a, January). E pur si muove: Galilean-invariant cosmological hydrodynamical simulations on a moving mesh. *MNRAS* *401*, 791–851.
- Springel, V. (2010b, September). Smoothed Particle Hydrodynamics in Astrophysics. *ARAAS* *48*, 391–430.
- Springel, V., T. Di Matteo, and L. Hernquist (2005, August). Modelling feedback from stars and black holes in galaxy mergers. *MNRAS* *361*, 776–794.
- Springel, V., S. D. M. White, A. Jenkins, C. S. Frenk, N. Yoshida, L. Gao, J. Navarro, R. Thacker, D. Croton, J. Helly, J. A. Peacock, S. Cole, P. Thomas, H. Couchman, A. Evrard, J. Colberg, and F. Pearce (2005, June). Simulations of the formation, evolution and clustering of galaxies and quasars. *Nature* *435*, 629–636.

- Springel, V., N. Yoshida, and S. D. M. White (2001, April). GADGET: a code for collisionless and gasdynamical cosmological simulations. *NATURE* 6, 79–117.
- Stevenson, J. B., L. J. King, and J. Donaghey (In prep). Parameter constraints of Abell 2146 using Dawson’s code. *MNRAS*.
- Teyssier, R. (2002, April). Cosmological hydrodynamics with adaptive mesh refinement. A new high resolution code called RAMSES. *Astronomy and Astrophysics* 385, 337–364.
- Trotta, R. (2008, March). Bayes in the sky: Bayesian inference and model selection in cosmology. *Contemporary Physics* 49, 71–104.
- White, J. A., R. E. A. Canning, L. J. King, B. E. Lee, H. R. Russell, S. A. Baum, D. I. Clowe, J. E. Coleman, M. Donahue, A. C. Edge, A. C. Fabian, R. M. Johnstone, B. R. McNamara, C. P. O’Dea, and J. S. Sanders (2015, November). Dynamical analysis of galaxy cluster merger Abell 2146. *MNRAS* 453, 2718–2730.
- Zitrin, A., M. Meneghetti, K. Umetsu, T. Broadhurst, M. Bartelmann, R. Bouwens, L. Bradley, M. Carrasco, D. Coe, H. Ford, D. Kelson, A. M. Koekemoer, E. Medezinski, J. Moustakas, L. A. Moustakas, M. Nonino, M. Postman, P. Rosati, G. Seidel, S. Seitz, I. Sendra, X. Shu, J. Vega, and W. Zheng (2013, January). CLASH: The Enhanced Lensing Efficiency of the Highly Elongated Merging Cluster MACS J0416.1-2403. *ApJ* 762, L30.

BIOGRAPHICAL SKETCH

Joseph E. Coleman moved to Texas 19 years ago. He worked doing odd jobs in the tech industry. This allowed for travel all over the United States and he got to see and visit many scientific sites. He enjoys science tourism and has been to the Arecibo Observatory in Puerto Rico, the Very Large Array in New Mexico, Biosphere 2 in Arizona, the Trinity Site in New Mexico, Los Alamos National Labs in New Mexico, McDonald Observatory in Texas, and the Laser Interferometer Gravitational-Wave Observatory in Washington.

After working in the technology industry for a while, he decided to complete a degree in Physics. He ended up getting two bachelor's degrees, one in physics, the other in mathematics.

The choice to pursue a doctorate degree was due in part to encouragement from his advisor, Dr. Lindsay King.

CURRICULUM VITAE

Joseph E. Coleman

May, 2018

Contact Information:

Department of Physics
The University of Texas at Dallas
800 W. Campbell Rd.
Richardson, TX 75080-3021, U.S.A.

Educational History:

M.S., Physics, The University of Texas at Dallas
B.S., Mathematics, The University of Texas at Dallas
B.S., Physics, The University of Texas at Dallas
A.S., Collin County Community College

Publications:

The mass distribution of the unusual merging cluster Abell 2146 from strong lensing. **Joseph E. Coleman**, Lindsay J. King, Masamune Oguri, Helen R. Russell, Rebecca E. A. Canning, Adrienne Leonard, Rebecca Santana, Jacob A. White, Stefi A. Baum, Douglas I. Clowe, Alastair Edge, Andrew C. Fabian, Brian R. McNamara, Christopher P. O’Dea *MNRAS*, 2017, *arXiv:1609.06765*

The distribution of dark and luminous matter in the unique galaxy cluster merger Abell 2146. King, Lindsay J.; Clowe, Douglas I.; **Coleman, Joseph E.**; Russell, Helen R.; Santana, Rebecca; White, Jacob A.; Canning, Rebecca E. A.; Deering, Nicole J.; Fabian, Andrew C.; Lee, Brandyn E.; Li, Baojiu; McNamara, Brian R. *MNRAS*, 2016, *arXiv:1609.06734*

Method and apparatus to perform online credential reporting. Gerald William Wineinger, Travis Jay Wineinger, **Joseph Eric Coleman**, Terry James Hegg *USPTO*, 2016

Dynamical analysis of galaxy cluster merger Abell 2146 White, J. A.; Canning, R. E. A.; King, L. J.; Lee, B. E.; Russell, H. R.; Baum, S. A.; Clowe, D. I.; **Coleman, J. E.**; Donahue, M.; Edge, A. C.; Fabian, A. C.; Johnstone, R. M.; McNamara, B. R.; O’Dea, C. P.; Sanders, J. S. *MNRAS*, 2015, *arXiv:1508.01505*

Awards and Scholarships:

2014-2017 Texas Space Grant Consortium Fellowship
2015 Tanveer and. M Yaqub Mirza Scholarship

2012-1013 Marsh W. White Outreach Award, Society of Physics Students
2012 Student Presentation Award, Texas Section of the American Physical Society
2010 NASA Community College Aerospace Scholar

Presentations and Talks:

2017, Gravitational Lensing and Hydrodynamic Simulation of Abell 2146, Mathematical Physics and General Relativity Symposium in Honor of Professor Ivor Robinson
2017, Mass Distribution from Strong Gravitational Lensing of Merging Cluster Abell 2146, 229th AAS Meeting
2012, Resonant Circuit Simulation and Development for LIGO Lasers, Texas Section of the APS Fall Meeting

Teaching:

2013-2017 Graduate Teaching Assistant, Mechanics Lab, Electricity and Magnetism, Astronomy, Graduate Electrodynamics 1 and 2
2014 Python Workshop, Gave a workshop introducing professors, graduate and undergraduate students to the programming language.
2012-2013 Undergraduate Teaching Assistant, Electricity and Magnetism Lab, Astronomy, Weather and Climate